Remote Control of Cell Signaling through Caveolae Mechanics

Satish Kailasam Mani[1,14], Nicolas Tardif[1,12,14], Olivier Rossier[2,3,14], Ismail Khater[4,5], Xuesi Zhou[2,3], Filipe Nunes Vicente[2,3], AV Radhakrishnan[2,3], Céline Gracia[1], Pamela Gonzalez Troncoso[1], Isabel Brito[6], Richard Ruez[1,13], Melissa Dewulf[1], Ghassan Hamarneh[4], Ivan Robert Nabi[7], Pierre Sens[8], Irina S. Moreira[9,10,11], Grégory Giannone[2,3,15], Cédric M. Blouin[1,15*] and Christophe Lamaze[1,15,16*]

[1] Institut Curie, PSL Research University, CNRS UMR3666, INSERM U1143, 75005 Paris, France

[2] Interdisciplinary Institute for Neuroscience, UMR 5297, University of Bordeaux, France.

[3] Interdisciplinary Institute for Neuroscience, UMR 5297, CNRS, Bordeaux, France.

[4] School of Computing Science, Simon Fraser University, Burnaby, BC V5A 1S6, Canada

[5] Department of Electrical and Computer Engineering, Faculty of Engineering and Technology, Birzeit University, Birzeit P627, Palestine

[6] Institut Curie, PSL University, INSERM U900, Mines Paris Tech, 75005 Paris, France

[7] Department of Cellular and Physiological Sciences, University of British Columbia, Vancouver, BC V6T 1Z3, Canada

[8] Institut Curie, PSL Research University, Sorbonne University, CNRS UMR168, 75005 Paris, France

[9] Department of Life Sciences, University of Coimbra, Calçada Martim de Freitas, 3000-456 Coimbra, Portugal

[10] CNC-UC - Center for Neuroscience and Cell Biology, University of Coimbra

[11] CIBB - Centre for Innovative Biomedicine and Biotechnology, University of Coimbra

[12] Present address: Glaxosmithkline, 92500 Rueil-Malmaison, France

[13] Present address: ALIRI Bioanalysis, 59120 Loos, France

[14] These authors contributed equally

[15] These authors contributed equally

[16] Lead contact

* Correspondence to: christophe.lamaze@curie.fr (C.L.), cedric.blouin@curie.fr (C.M.B.)

Abstract

Caveolae are invaginated plasma membrane nanodomains traditionally associated with membrane trafficking and signaling. These multifunctional organelles are also essential mechanosensors mediating the cell response to mechanical stress. We investigated the role of caveolae mechanics in regulating various signaling pathways. Single molecule imaging and super resolution microscopy revealed that mechanical stress rapidly triggers caveolae disassembly and the release of caveolin-1 scaffolds, which exhibit enhanced diffusion at the plasma membrane. This promoted direct interaction between the caveolin-1 scaffolding domain and the tyrosine kinase JAK1, leading to the inhibition of its catalytic activity. A similar process was observed for eNOS, PTEN, and PTP1B. Remote control of signaling by caveolae was validated by a theoretical model based on caveolae thermodynamics. These findings establish a novel mechanotransduction paradigm where signaling information is decoded remotely from the initial mechanosensing caveola, through dynamic and reversible assembly of tension-controlled complexes between signaling effectors and caveolin-1 scaffolds.

Main

Caveolae are discrete bulb shaped structures located at the plasma membrane with diameters ranging between 50-80 nm in diameter and that are occasionally clustered in 'rosettes' [1,2]. They were first identified through electron microscopy (EM) in epithelial and endothelial cells over 70 years ago [3,4]. The integral membrane protein caveolin-1 oligomerizes to form the primary 8S building blocks of caveolae assembly in many cell

types, particularly abundant in adipocytes, endothelial cells, and muscle cells. The caveolin family of proteins consist of three isoforms: caveolin-1 (Cav1), caveolin-2 (Cav2), and muscle-specific caveolin-3 (Cav3) [5-7]. Despite the presence of electron dense regions on their cytoplasmic face observed in early EM experiments, caveolae were traditionally described as non-coated invaginations, in contrast to the characteristic fuzzy coat seen on clathrin-coated pits. The composition and organization of the caveolar coat were ultimately elucidated with the discovery of the cavin family of cytosolic proteins, which include cavin1, cavin2, cavin3, and cavin4. Cavin1, is essential for caveolae morphogenesis in all cell types [8] while cavin4 expression is limited to muscle cells [9-11]. Several accessory proteins including EHD2, pacsin2/syndapin2 (pacsin3/syndapin3 in muscle cells), and filamin A have also been localized at the neck of caveolae and proposed to control caveolae stability and dynamics through interactions with the actin cytoskeleton [12-16]. In a recent cryo-EM study, the quaternary structure of the Cav1 complex was resolved [17]. The 8S complex has been proposed to consist of 11 primary α-helical protomers that are tightly packed into a 14 nm spiral disk. The N-termini are located on the outer ring, while the C-termini form a central cylindric β-barrel structure.

Multiple studies have investigated the role of caveolae and/or Cav1 in various vital biological processes, including transcytosis and endocytosis, lipid homeostasis, and signal transduction [18-21]. The diverse range of functions attributed to caveolae and their associated proteins accounts for their involvement in several human diseases. For example, mutations or impaired expression of caveolins and cavins have been associated with lipodystrophy, vascular dysfunction, cancer, and muscle dystrophies [22-25].

The most explored function of Cav1 concerns the regulation of intracellular signal transduction [1,26,27]. Earlier studies have proposed that caveolae and/or Cav1 can modulate the activity of various growth factors, signaling receptors, and kinases. These include endothelial nitric oxide synthase (eNOS), insulin receptor, epidermal growth factor receptor (EGFR), src-like kinases, H-ras and K-ras [28-32]. Difficulties to unambiguously localize these signaling effectors into caveolae has however questioned the reliability of these studies which were primarily based on overexpression of signaling proteins and Cav1, possibly leading to localization artefacts. Consequently, caveolae were found to exclude bulk plasma membrane protein with transmembrane and cytosolic domains, and instead to concentrate membrane lipids [33].In this context, a role for Cav1 in controlling signaling outside of caveolae was proposed based on the ability of endogenous Cav1 to inhibit EGFR signaling in tumor cells that lack caveolae [34]. Subsequent studies have shown that Cav1 controls cancer cell migration and tumor progression by regulating focal adhesion signaling and tension in prostate cancer PC3 cells that lack cavin1 and therefore caveolae [9,35-37]. These non-caveolar Cav1 assemblies were termed scaffolds [38] and were recently visualized at the plasma membrane by single molecule localization super-resolution microscopy [39,40] and by EM [41]. The question of how the central function of Cav1 in caveolae morphogenesis relates to its control over the activity of signaling receptors that are not located within caveolae is unresolved, making it an essential area of research.

In 2011, we uncovered a novel function of caveolae in mechano-sensing. Upon exposure to mechanical stress, caveolar invaginations undergo rapid flattening within the plasma membrane to expand membrane area, effectively acting as a buffer against sudden increases in membrane tension, thereby protecting the plasma membrane

against rupture [42]. This essential role of caveolae in cell mechanics was further confirmed in several cell types *in vitro* and *in vivo* [41,43-47]. The new role of caveolae in cell mechanics has prompted a re-evaluation of their conventional functions, and there is now a consensus that caveolae need to be revisited in light of this new understanding [2,48-51].

Here, we investigated the effects of the tension-dependent cycle of caveolae disassembly and reassembly on intracellular signaling. We performed high-throughput reverse phase protein array analysis on cells subjected to mechanical stress and identified several signaling pathway that were directly controlled by caveolae mechanics. Using super resolution microscopy and live-cell single molecule imaging, we found that in response to mechanical stress, caveolae rapidly disassembled into smaller Cav1 assemblies corresponding to scaffolds [39,40]. The pool of released Cav1 scaffolds was found to diffuse rapidly in the plasma membrane and to directly interact through their scaffolding domain with several signaling effectors outside of caveolae, including the Janus kinase JAK1. As a result, JAK1 catalytic activity was inhibited as shown by the lack of STAT3 activation by interferon-α. Upon stress release, JAK-STAT activation by IFN-α resumed to normal levels. Computational protein-protein docking experiments confirmed the interaction of the caveolin 8S complex with the JAK1 catalytic domain and identified the key residues involved in this interaction. We could extend the mechanical regulation of signaling by Cav1 scaffolds to PTEN and PTP1B tyrosine phosphatases, and to eNOS. A theoretical model based on the thermodynamics of caveolae assembly and disassembly under mechanical stress could recapitulate these observations and further establish the generality of the proposed remote signaling mechanism. Altogether, our

study provides a new paradigm in mechanotransduction by which selective signaling pathways are remotely controlled at locations distant from budded caveolae.

Results

Several signaling pathways are controlled by caveolae under mechanical stress

Our primary objective was to investigate whether the mechano-dependent cycle of caveolae disassembly and reassembly could serve as a mechanical switch, potentially enabling caveolae and /or caveolins to modulate specific signaling pathways [1,48]. For this, we conducted a high-throughput screening experiment using reverse phase protein array (RPPA) – a miniaturized dot-blot technology that enables proteomic analysis and identification of activated or altered signaling pathways [52]. The RPPA analysis was performed on wild-type (WT) and Cav1 knockout (*CAV1*$^{-/-}$) mouse lung endothelial cells (MLEC) subjected to uniaxial stretching. Cells were also stimulated with IFN-α or IFN-β to extend the analysis to the JAK/STAT signaling pathway (Figure 1A). Several signaling pathways were affected as exemplified by the stretch-dependent threonine phosphorylation of MAPK and serine phosphorylation of AKT kinases (Figure 1B). While certain signaling pathways, such as MAPK, were activated by stretch irrespective of the presence of Cav1, the significant upregulation in AKT phosphorylation on serine 473 (pSer473) triggered by uni-axial stretching required Cav1. Meanwhile, the level of PKC-α activation (pSer657) was not affected by stretching in WT MLEC cells (Figure 1B). As anticipated, our RPPA analysis confirmed that stimulation with IFN-α resulted in the phosphorylation of STAT3 at tyrosine 705 (Tyr705 pSTAT3) and STAT1 at tyrosine 701 (Tyr701 pSTAT1) (Figure 1C). When cells were subjected to stretching in the presence

of IFN-α, there was a significant reduction in the level of STAT3 phosphorylation, which in turn was dependent on the presence of Cav1. However, the phosphorylation of STAT1 remained unaffected under these conditions (Figure 1D). These observations underscore the involvement of caveolae and/or Cav1 in the mechano-regulation of specific signaling pathways.

The validity of our RPPA analysis findings was confirmed by Western blot analysis in MLEC WT and MLEC *CAV1*$^{-/-}$ cells that were stimulated with IFN-α under 25% uniaxial stretching conditions. We measured a 43% decrease in pSTAT3 levels in stretched cells as compared to non-stretched or resting cells (Figure 1E). No activation of STAT3 was measurable in the absence of IFN-α stimulation in both cell types (Extended data figure 1F). Consistent with the RPPA analysis, the level of STAT3 tyrosine phosphorylation was found to be unaltered in MLEC *CAV1*$^{-/-}$ cells that were subjected to stretch, further confirming that this regulatory mechanism is dependent on the presence of functional caveolae and/or Cav1 (Figure 1E). Consequently, the reduction in STAT3 phosphorylation levels resulted in a corresponding inhibition of STAT3 nuclear translocation in stretched cells (Figure 1F). Again, under these conditions, we found that STAT1 nuclear translocation remained unaffected. Similarly, the level of pSTAT3 in the nucleus was not affected by stretch in MLEC *CAV1*$^{-/-}$ cells (Figure 1F). These results strongly suggest the involvement of caveolae and/or Cav1 in the specific modulation of STAT3 phosphorylation levels in response to mechanical stress.

Interaction of Cav1 with JAK1 results in STAT3 inhibition

The activation of JAK-STAT signaling by IFN-α depends on the ubiquitous IFNAR receptor, which consists of two receptor subunits, IFNAR1 and IFNAR2 [53]. STAT3 is a direct cytosolic downstream effector of TYK2 and JAK1 tyrosine kinases, which are associated with IFNAR1 and IFNAR2, respectively. We hypothesized that the modulation of STAT3 tyrosine phosphorylation by caveolae/Cav1 in response to mechanical stress could be mediated through the interaction of Cav1 with JAK1 or TYK2. Treatment of cells with a hypo-osmotic medium (30 mOsm) for 5 minutes results in increased membrane tension due to cell swelling and leads to rapid caveolae disassembly, similar to the response observed during cell stretching [42]. Co-immunoprecipitation (co-IP) of both endogenous Cav1 and JAK1 was performed on MLEC WT and MLEC *CAV1*$^{-/-}$ cells subjected to hypo-osmotic shock. We found that Cav1 interacts with JAK1 in resting cells, and this interaction is significantly increased by up to 3-fold in response to mechanical stress, such as hypo-osmotic shock (Figure 2A). We repeated the co-IP experiment with IFN-α stimulation to assess the effect of increased Cav1-JAK1 interaction on STAT3 phosphorylation. The increase in interaction between Cav1 and JAK1, induced by hypo-osmotic shock, was correlated with a substantial reduction of up to 62% in STAT3 phosphorylation levels (Figure 2B). Remarkably, during the recovery phase when caveolae had reassembled to their initial numbers upon returning to iso-osmotic conditions [42], we observed that both the levels of Cav1 interaction with JAK1 and IFN-α-induced STAT3 phosphorylation reverted to the levels measured in the resting state. We also measured a higher level of STAT3 phosphorylation in MLEC *CAV1*$^{-/-}$ cells, in agreement with the known regulation of STAT3 activity by Cav1 [54,55]. These data suggest that the amount of Cav1 released from caveolae during mechanical disassembly can

control the degree of Cav1-JAK1 interaction, which in turn can regulate STAT3 phosphorylation. This process is reversible and governed by mechanical stress. TYK2 was not detected in the co-immunoprecipitates with Cav1, indicating that there is no interaction between Cav1 and TYK2 in this process (Extended data figure 1D).

The caveolin scaffolding domain mediates the interaction between Cav1 and JAK1

STAT3 activation by IFN-α was inversely correlated with the level of Cav1 interaction with JAK1 suggesting that Cav1 can act as a negative modulator of JAK1 activity and thereby, STAT3 phosphorylation. The caveolin scaffolding domain (CSD), consisting of NH_2-terminal residues 82-101 of Cav1, has been proposed to bind specifically to a limited set of signaling effectors mainly to exert an inhibitory effect [28,29,56,57]. To investigate whether the CSD is responsible for the interaction between Cav1 and JAK1, we expressed a Cav1 construct with point-mutations inactivating the Phe92 and Val94 residues (Cav1-RFP F92A/V94A) in MLEC *CAV1*$^{-/-}$ cells. In cells expressing Cav1 F92A/V94A, JAK1 was not detected in the immunoprecipitated fractions, whereas it was found to co-precipitate with Cav1 WT (Figure 3A and Extended data figure 1D).

We also monitored the level of pSTAT3 nuclear translocation induced by IFN-α stimulation in MLEC *CAV1*$^{-/-}$ cells re-expressing either Cav1 WT or Cav1 F92A/V94A (Figure 3B). The level of pSTAT3 nuclear translocation was comparable between MLEC *CAV1*$^{-/-}$ cells expressing Cav1 WT and MLEC WT cells (Extended data figure 1A). Furthermore, expression of either Cav1 WT or Cav1 F92A/V94A had no effect of the level of basal STAT3 (Extended data figure 1B). In non-transfected cells, pSTAT3 nuclear translocation occurred normally; however, in cells overexpressing Cav1 WT, a lack of

pSTAT3 nuclear translocation was observed, supporting the inhibitory effect of Cav1 on JAK1 activity. In cells expressing the F92A/V94A mutated Cav1 CSD, the nuclear translocation of pSTAT3 was restored upon IFN-α stimulation, indicating that the inability of F92A/V94A Cav1 to negatively regulate STAT3 activation was presumably due to its inability to interact with JAK1 (Figure 3A and 3B). In agreement with the insensitivity of STAT1 activation to mechanical stress and caveolae, the nuclear translocation of pSTAT1 induced by IFN-α was unaffected, regardless of whether cells express Cav1 WT or Cav1 F92A/V94A (Extended data figure 1C).

We further investigated the function of the Cav1 CSD using two peptides that mimic the CSD, the CavTratin peptide corresponding to the Cav1 CSD (Cav1 ^{82}DGIWKASF**TTF**TVTKYWFYR^{101}) and a peptide named CavNoxin (Cav1 ^{82}DGIWKASF**AAA**TVTKYWFYR^{101}) where key amino acids of the CSD are replaced by alanines, thus abolishing its inhibitory action [58]. Upon treatment of MLEC WT with CavTratin, we observed a significant decrease of pSTAT3 levels upon IFN-α stimulation, as compared to cells treated with a control scrambled peptide (Figure 3C), indicating that the CSD domain of Cav1 is sufficient for negatively regulating STAT3 activation. Conversely, cells treated with CavNoxin showed a significant increase of IFN-α-induced pSTAT3. Overexpression of Cav1 can generate a pool of non-caveolar Cav1 at the plasma membrane presumably due to an imbalance in the stoichiometry between the number of Cav1 molecules and the other caveolar components required for caveolae assembly, most likely cavin-1 [36,59]. Conversely, the mutated Cav1 CSD peptide CavNoxin relieves JAK1 inhibition, most likely by competing or associating with endogenous Cav1. To exclude the possibility of the involvement of an unknown third-party interacting partner,

we directly assessed the impact of CSD binding on JAK1's ability to catalyze ATP hydrolysis in a cell free assay. The catalytic activity of human recombinant JAK1 as measured by the conversion of ATP to ADP was maintained with increasing concentrations of the control peptide. In contrast, the addition of CavTratin to the reaction mix resulted in a significant and dose dependent decrease of ADP production by JAK1 (Figure 3D).

Several Cav1-interacting proteins have been shown to contain a consensus motif known as the caveolin binding motif (CBM) which is believed to be recognized by the CSD [60,61]. Since the presence of putative CBMs had not been reported in JAK1 kinase, we searched for such motifs by drawing analogies with known CBMs. Upon sequence analysis of JAK1, we identify three sequences as potential candidates: one within the FERM domain (^{157}YLFAQGQY^{164}), another in the pseudokinase domain (^{777}WSFGTTLW^{784}), and a third within the tyrosine kinase domain (^{1065}WSFGVTLH^{1072}). We ruled out the first sequence as it is not present in the recombinant JAK1 used to measure JAK1 catalytic activity *in vitro* (Figure 3D). Co-immunoprecipitation experiments revealed that the sequence 1065-1072, and not the sequence 777-784, was required for the interaction between JAK1 and endogenous Cav1 (Extended data figure 1E). Altogether, these data highlight the essential role of the CSD in mediating the direct interaction between Cav1 and JAK1, most likely through binding to a motif located in the tyrosine kinase domain of JAK1. This interaction leads to a dose-dependent inhibitory effect of Cav1 on JAK1 catalytic activity and subsequent downstream signal transduction.

We next conducted docking experiments to characterize the protein-protein binding interface between Cav1 and JAK1. We explored the direct binding between the CSD of

Cav1, particularly focusing on the T90-V94 region, and the key regions of JAK1, retrieved from our experimental data (Extended data figure 1E). We employed an Information-Guided Docking approach to narrow the search space to probable binding sites, thereby enhancing the precision and relevance of the simulation results. Furthermore, our approach was meticulously designed to meet experimental criteria while adhering to crucial aspects of protein-protein interface dynamics in signal transduction. The critical aspect is the measurement of the Buried Surface Area (BSA), which is essential for quantifying the extent of interaction between the two proteins [62]. Additionally, we measured the number of pairwise contacts, where higher values indicate stronger interaction. Proper positioning of the membrane protein Cav1 relative to its soluble partner JAK1 was crucial to ensure the biological relevance of observed interactions. These parameters were evaluated across 200 potential docking decoys to enhance the statistical robustness of our findings. We selected the structure shown in Figure 4, which illustrates that Cav1-CSD ^{82}DGIWKASFTTFTVTKYWFYR^{101} is directly involved in binding to specific regions of JAK1, particularly residues E1029-Y1034 and E1051-Y1059. Notably, within these regions, the tyrosine residue Y1059 serves as the key interaction point, underscoring its crucial role in the binding interface between Cav1 and JAK1. JAK1 residues E1029-Y1034 and E1051-Y1059 primarily interacted with Cav1 residues T90, V94, and W98, underscoring the effectiveness of this docking decoy. This decoy was reproduced in the JAK1$\Delta^{1072\text{-}1154}$ variant in similar positions.

Furthermore, in the Cav1 complex with JAK1 WT, additional interactions were observed between specific residues in the JAK1 C-terminus (T1102-E1110 and F1134-P1136) and the S80-K86 region of a second Cav1 α-helical protomer. However, these

interactions do not significantly impact the binding affinity. The JAK1$\Delta^{1072\text{-}1154}$ variant, lacking these additional interactions, still effectively binds to Cav1. This underscores the crucial role of the primary Cav1 α-helical protomer in stabilizing the JAK1-Cav1 interface.

Multiple signaling pathways are controlled by the mechanical release of Cav1

In addition to JAK-STAT signaling, RPPA analysis revealed several other signaling pathways that were also modulated by cell stretching in a Cav1-dependent manner (Figure 1A). Under resting conditions, we performed co-immunoprecipitation experiments, which confirmed the previously reported interaction between endogenous Cav1 and endothelial nitric oxide synthase (eNOS) as well as protein tyrosine phosphatase 1B (PTP1B) (Figure 2C) [30,63]. The interaction between Cav1 and eNOS, as well as between Cav1 and PTP1B, was significantly enhanced during hypo-osmotic shock and returned to basal levels upon returning to iso-osmotic conditions. Additionally, we confirmed the interaction between Cav1 and phosphatase and tensin homolog (PTEN), a potent tumor suppressor gene that functions as a negative regulator of the AKT signaling pathway [64] (Figure 2D). Notably, during hypo-osmotic shock, the increased binding of Cav1 to PTEN correlated with an increase in AKT activation, indicated by serine 473 phosphorylation. The increase in AKT activity, also observed after cell stretching (Figure 1B), is likely a result of the inhibition of PTEN phosphatase activity by Cav1. As observed for JAK1, Cav1 interaction with PTEN required the Cav1-CSD domain (Extended data figure 1D). Similar to the interactions observed with JAK1, eNOS, and PTP1B, the interaction between Cav1 and PTEN returned to basal levels upon restoration of iso-osmotic conditions (Figure 2D). The level of pAKT, although significantly decreased upon return to iso-osmotic conditions, did not return to the initial level measured under

iso-osmotic conditions. This is likely due to the delay required for PTEN to be freed from Cav1 scaffolds before dephosphorylating pAKT. Furthermore, our observations revealed a significant correlation between the strength of the hypo-osmotic shock and the intensity of Cav1 interaction with JAK1, eNOS, and PTP1B. This increased interaction most likely reflects the increase of Cav1 molecules released from disassembled caveolae (Extended data figure 2A). Notably, this effect was rapid, with the maximum interaction observed after only 5 min of hypo-osmotic shock and did not further increase with longer exposure times (Extended data figure 2B and 2C). As reported earlier, Cav1 did not interact with TYK2, another member of the JAK family that is also activated by IFN-α. Caveolae and integrins have been shown to cooperate in the regulation of mechanosignaling [65]. We also recently established a reciprocal control between caveolae and integrins that is crucial for invadosome biogenesis and activity [66]. However, we could not immunoprecipitate integrins with Cav1 in MLEC cells (Extended data figure 2D). These results confirm the selectivity of caveolae mechanosignaling.

Mechanical stress enhances diffusion of Cav1 oligomers at the plasma membrane

We have initially hypothesized that the disassembly of caveolae in response to increased membrane tension would release non caveolar caveolins at the PM and coat proteins into the cytosol [42,48]. Indeed, single-molecule fluorescence analysis had revealed that caveolae flattening induced by membrane tension surges results in the disassembly of the cavin coat into two distinct cavin-1/cavin-2 and cavin-1/cavin-3 cytosolic sub-complexes [42,67]. In addition, we showed that an increase in membrane tension causes the EHD2 ATPase to be released from disassembled caveolae and translocated to the

nucleus where it regulates gene transcription [68]. The comprehension of the topology of Cav1 oligomers released upon caveolae flattening is crucial for understanding the functions of caveolae, but it is still limited. Caveolins could remain organized as a flat caveolar structure, as observed by deep-etch electron microscopy [42], or be released as non-caveolar Cav1 oligomers. Indeed, FRAP experiments have showed an increased mobile fraction of Cav1 upon mechanical stress, suggesting that a higher number of Cav1 molecules are freely diffusing outside of caveolae as reported by Sinha et al. in 2011 [42]. Therefore, we aimed to investigate the kinetics and dynamics of Cav1 molecules in response to mechanical stress. To monitor the fate of single Cav1 molecules with high spatiotemporal resolution at the PM, we performed single particle tracking (spt) coupled with photoactivation localization microscopy (PALM) using total internal reflection fluorescence microscopy (TIRF) [69-71]. By fusing Cav1 with the photo-switchable mEos3.2 fluorophore, we were able to conduct high frequency sptPALM acquisitions (50 Hz) and to analyze thousands of reconstructed mEos3.2-Cav1 trajectories. Cav1 trajectories were sorted according to their diffusion mode (diffusive, confined or immobile; Figure 5A), and diffusion coefficients (D) were computed (Figure 5B; Methods).

During the resting state, mEos3.2-Cav1 displayed a large fraction of immobile trajectories primarily confined to static mEos3.2-Cav1 structures, indicating that they are most likely confined within *bona fide* caveolae (Figure 5A, 5B and Movie 1). When we induced an acute increase in membrane tension through hypo-osmotic shock, we observed a dramatic increase in the fraction of diffusive mEos3.2-Cav1 trajectories that displayed fast free diffusion (Figure 5A, 5B and Movie 2). Importantly, the population of diffusive mEos3.2-Cav1 trajectories increased with the duration of the hypo-osmotic

shock (Figure 5C), in agreement with the visualization that mEos3.2-Cav1 trajectories explored a wider area with time. Furthermore, after subjecting cells to a hypo-osmotic shock and then returning them to iso-osmotic conditions (i.e., recovery), the population of diffusive mEos3.2-Cav1 decreased to levels similar to those recorded during the resting state (Figure 5D). This suggests that the disassembly process is reversible and that Cav1 molecules become immobilized again within caveolae upon their reassembly. Notably, the hypo-osmotic shock did not affect the diffusion of a plasma membrane targeting sequence containing the CAAX motif (CAAX-mEos3.2), which was used as a control for bulk membrane dynamics (Extended data figure 3A). Taken together, these results indicate that in response to mechanical stress, Cav1 molecules initially immobilized within caveolae are released into the PM in a highly dynamic and reversible manner, as evidenced by the kinetics of their trajectories.

Cav1 oligomers interact with JAK1 to modulate the JAK-STAT pathway

Differentiating between the functions of caveolae and caveolin oligomers in various cellular processes has been a persistent challenge in the field of caveolae [1,2,38,72]. In this context, we aimed to investigate whether the pool of Cav1 that interacts with JAK1 in response to changes in membrane tension is non-caveolar in nature. When cavin1 is absent, Cav1 is unable to assemble into morphologically distinguishable caveolae and remains instead as a pool of non-caveolar Cav1 with increased lateral mobility within the plasma membrane [9]. Indeed, we used mouse embryonic fibroblasts knocked out for the *PTRF* gene encoding cavin1 (MEF Cavin1$^{-/-}$) and conducted sptPALM microscopy. We observed a higher fraction of the diffusive mEos3.2-Cav1 trajectories that displayed faster

free diffusion in MEF cells devoid of Cavin1 (Figure 5E, 5G and 5H). It is noteworthy that the proportion of diffusive and immobile Cav1 molecules, as well as the diffusion coefficients, were similar to those measured in WT MEF cells during hypo-osmotic shock (Figure 5F and 5H). The exogenous expression of Cavin1, which allows *de novo* formation of caveolae in these cells, had a major effect on the diffusion parameters of Cav1 molecules, as it drastically reduced the fraction of diffusive Cav1 molecules to levels similar to that measured in WT MEF cells at rest (Figure 5E, 5F, 5G and 5H). We next investigated the impact of highly diffusive Cav1 molecules on JAK/STAT signaling. For this, we measured the level of STAT3 phosphorylation in MEF Cavin1$^{-/-}$ cells stimulated or not with IFN-α. As expected, unstimulated cells did not exhibit any activation of STAT3 (Figure 5I). While the stimulation of MEF Cavin1$^{-/-}$ cells by IFN-α failed to activate STAT3, the reintroduction of cavin1 in these cells was sufficient to restore the IFN-α-induced activation of STAT3 (Figure 5I). Finally, we used MEF Cavin1$^{-/-}$ cells re-expressing different levels of Cav1 oligomers and found an inverse correlation between the amount of Cav1 oligomers present in the cells and the level of STAT3 activation (Figure 5J). These results strongly suggest that non-caveolar Cav1 is solely responsible for the inhibition of STAT3 activation by IFN-α.

Nanoscale imaging of Cav1 oligomers under mechanical stress

Recent advancements in super-resolution microscopy and machine-learning have provided novel insights into the nanoscale organization of various subcellular structures [73-78]. We used stochastic optical reconstruction microscopy (STORM) to capture images of endogenous Cav1 and Cavin1 in MLEC cells and could visualize circular structures

with an apparent diameter ranging from 50-100 nm, which is consistent with the known size of caveolae (Figure 6A, Extended data figure 4A and 4B). In addition, the use of an astigmatic lens with HILO illumination allowed to visualize caveolae in the three-dimensional space (Extended data figure 4C). The disassembly of caveolae during hypo-osmotic shock is likely a two-step process in which budded caveolae first flatten out before completely releasing the coat components [42]. Consistent with this, the observed diameter of certain Cav1-positive structures, as indicated by their fluorescent intensity profiles, increases from 80 nm to 120 nm during hypo-osmotic shock, probably reflecting the flattening of caveolae. Upon returning to iso-osmotic conditions (recovery), the diameter of caveolae decreased to their normal size i.e. 70 nm, as expected from the reassembly of *bona fide* budded caveolae (Extended data figure 4A).

It has been proposed that Cav1 forms oligomers outside of caveolae, assembling into what are referred to as Cav1 scaffolds [38]. However, these scaffolds are not visually detectable using conventional fluorescence microscopy or electron microscopy techniques. Recently, multi-proximity threshold network analysis was applied to single molecule localization microscopy (SMLM) data acquired from PC3 cells that naturally lack cavin1 and from cavin1 transfected PC3 cells. This study allowed the classification of caveolae along with three distinct classes of Cav1 scaffolds. The classification was achieved using weakly supervised machine learning through cluster-based feature analysis, taking into account various parameters including size, shape, topology, hollowness, network characteristics, and oligomerization state [39]. The smallest S1A scaffold is proposed to correspond to the previously identified 8S complex of SDS-resistant 11 Cav1 protomers, which are the minimal building blocks required to assemble

the final 70S complex of budded caveolae [17,59,79]. It has been proposed that the smallest S1A scaffolds can dimerize to form S1B scaffolds, whereas larger S2 scaffolds would correspond to a hemispherical intermediate made of several S1A scaffolds (Figure 6A) [40]. We applied the same computational network modeling and machine learning based 3D pattern analysis to 3D STORM Cav1 localizations to enable the nanoscopic identification and visualization of caveolae and Cav1 scaffolds in resting MLEC WT cells. In addition to identifying *bona fide* caveolae, our post cluster segmentation allowed the visualization of numerous S1A, S1B and S2 Cav1 scaffolds (Figure 6B). Based on the recent cryo-electron microscopy structure of human Cav1 at 3.5 Å, the minimal 8S assembly complex is composed of 11 Cav1 protomers [17]. Previous quantitative TIRF studies have estimated that there are 144 ± 39 Cav1 copies per caveola [80], suggesting that *bona fide* caveolae are likely assembled by thirteen 8S complexes or S1A scaffolds [40]. By extrapolating these estimates to our own data, we found that in resting cells, approximatively 49% of Cav1 molecules were present in caveolae, while the mean number of Cav1 molecules in S2 scaffolds, S1B scaffolds and S1A scaffolds accounted for 30%, 14%, and 7%, respectively (Table 2). We examined the impact of mechanical stress on the distribution of caveolae and Cav1 scaffolds and observed a rapid and drastic effect upon 5 min hypo-osmotic shock. While the number of budded caveolae decreased by about 34% in line with our previous findings [42], we observed a concomitant increase in the number of Cav1 scaffolds, particularly in the S1A and S1B populations, which increased by 20% and 30%, respectively (Figure 6C and Table 1).

To ensure the accuracy and reliability of the results, it was important to confirm these data using another super resolution microscopy technique. To this end, we employed DNA-

based point accumulation for imaging in nanoscale topography (DNA-PAINT) to visualize the different Cav1 populations. DNA-PAINT relies on the stochastic binding of a fluorescent single-stranded DNA (imager strand) to the target-bound complement (docking strand) with sub-10 nm spatial resolutions [81]. To image Cav1, we used an anti-GFP nanobody that was functionalized with a DNA strand in MLEC *CAV1*$^{-/-}$ cells expressing Cav1-GFP. We performed DNA-PAINT to achieve super resolution imaging and investigate the structural organization of the different Cav1 populations at rest and after live cyclic stretching using a stretching device compatible with super-resolution microscopy [81]. At rest, we were able to discern two broad and distinct distributions of nano-objects. The first and larger population (54%), with a size above 70 nm, is likely to correspond to *bona fide* caveolae. The second population comprising 46% of the total and with a size below 70 nm, is likely to represent Cav1 scaffolds (Figure 6D). After subjecting the cells to a 30% live uni-axial cyclic stretching at a frequency of 0.5 Hz for 30 min, we observed a significant increase in the population of Cav1 scaffolds, which now represent 64% of the total Cav1 structures (Figure 6D). This occurred at the expense of *bona fide* caveolae, similar to what was observed by 3D STORM during hypo-osmotic shock experiments (Figure 6C). The smallest Cav1-GFP structures detected using DNA-PAINT have sizes of around 25 nm, which exceeds the experimental spatial resolution. This suggests that the smallest caveolar entities detected by DNA-PAINT are S1A scaffolds and not individual caveolins. Altogether, these data confirm that membrane tension surges induced by cell swelling or cyclic stretching lead to a reduction in *bona fide* caveolae. Furthermore, we demonstrate that caveolae flattening and disassembly are followed by the release of Cav1 oligomers that are assembled into scaffolds.

Preferential interaction of S1A and S1B Cav1 scaffolds with JAK1 under mechanical stress

Next, we investigated whether there were preferential interactions between any of the Cav1 scaffolds and JAK1 in response to mechanical stress. For this, we used multicolor 3D STORM combined with spectral demixing to localize endogenous Cav1 and JAK1 proteins simultaneously (Extended data figure figure 4B and 4D). We then applied machine learning and network features-based analysis to categorize Cav1 clusters and visualize them as caveolae and Cav1 scaffolds. Next, we analyzed the interaction between Cav1 clusters and JAK1 based on their nanoscale proximity in MLEC cells at steady state, as well as in cells subjected to a 5-minute hypo-osmotic shock. Analysis of the interaction strength using the MosaicIA plugin [82] revealed a significant increase in the interaction index/score of JAK1 with the S1A and S1B scaffolds in response to hypo-osmotic shock, while the interaction with caveolae and S2 scaffolds remained minimal and unchanged (Figure 6E, Extended data figure 4E). Furthermore, we generated objects of JAK1 and Cav1 clusters using PoCA software and used their centroids to calculate the distance between pairs of objects (i.e. between JAK1-Caveolae, JAK1-S2, JAK1-S1B and JAK1-S1A) (Figure 6E). The analysis of the occurrence of object pairs being at a distance less than 100 nm within a defined ROI corroborates our findings from the interaction analysis wherein the non-caveolar scaffolds S1B and S1A demonstrate increased proximity to JAK1 in response to hypo-osmotic shock (Extended data figure 4F). We can speculate that at rest, Cav1 molecules may be shielded from its interaction with JAK1 when they are mainly assembled into caveolae or S2 scaffolds. Hypo-osmotic shock or

stretching can significantly increase the proportion of highly diffusive Cav1 as S1A and S1B scaffolds. These scaffolds may be more accessible to JAK1, leading to a physical encounter between the two proteins. These results suggest that changes in membrane tension regulate the proportion of caveolae and Cav1 scaffolds at the plasma membrane. Cav1 scaffolds are more diffusive than caveolae and have exposed CSDs [17], which promote their interaction with JAK1 to negatively regulate the JAK/STAT signaling pathway.

Physical model of caveolae formation under mechanical stress

We developed a theoretical model of caveolae self-assembly based on our observations (Supplementary Note 1). The model is based on equilibrium thermodynamics [83], owing to the reversibility of caveolae disruption under stress. The model accounts for the presence of full caveolae and hemispherical S2 scaffolds, together with smaller S1 scaffolds accounting for both S1A and S1B (Figure 7A). Minimization of the system's free energy (detailed in Supplementary Note 1), yields a membrane tension-dependent fraction of the total Cav1 population in the different states, which is proportional to

$$caveolae\colon \rho_{full} = n\, e^{n(\mu_c + e_b - \sigma)} \quad S2\colon\ \rho_{half} = \frac{n}{2}\, e^{\frac{n}{2}(\mu_c + e_b + \lambda - \frac{\sigma}{2})} \quad S1\colon \rho_1 = e^{\mu_c} \qquad (1)$$

where σ is the membrane tension, e_b is the binding energy between S1 scaffolds in larger domains (caveolae and S2), λ is the line tension associated with the boundaries of S2 domains, $n = 13$ is the number of S1 in caveolae and μ_c is the Cav1 chemical potential, obtained from the conservation of the total number of Cav1 at the membrane (see below). The energetic parameters are normalized to be expressed in unit of the thermal energy $k_B T$.

The model predicts that the fraction of Cav1 in caveolae decreases while the fraction of freely diffusing Cav1 increases in sigmoidal fashions with the membrane tension (Figure 7B). Hemispherical S2 domains exist within a limited range of membrane tension, that strongly depends on the S2 line tension. The parameters of Figure 7B are fitted to reproduce the different populations observed by super resolution (Figure 6B and 6E). Although the fit is not unique, it nevertheless suggests that the homeostatic value of the membrane tension is within the range that permits substantial variation of free Cav1 under stretch. Free Cav1 may interact with membrane-associated signaling effectors, leading to their inactivation. This is described within the same framework, where the population of effectors in the different states is proportional to

$$active: \rho_j = e^{\mu_j} \quad inactive\ (bound\ to\ Cav1): \rho_d = e^{\mu_j+\varepsilon+\mu_c} \qquad (2)$$

where ε is the binding energy between S1 and effectors, and μ_j is the effector chemical potential. The two chemical potentials are obtained from the conservation of the total number of the respective proteins at the membrane: $\rho_1 + \rho_d + \rho_{full} + \rho_{half} = \rho_{tot}$ and $\rho_j + \rho_d = \rho_{j,tot}$. Membrane tension increase leads to effector inactivation by releasing Cav1 from caveolae and S2 aggregates (Figure 7C). A more complete version of the model developed in the Supplementary Note 1 allowing for the binding of multiple effectors on free Cav1 oligomers does not qualitatively affect the picture shown in Figure 7B and 7C. Therefore, our model, based on equilibrium thermodynamics, predicts how the population of different Cav1 states varies with membrane tension and yields a quantification of remote control of signaling by caveolae. It allows to reproduce our experimental conclusions, made on the basal surface of adhered cells subjected to an

535 osmotic shock, but also to propose quantitative predictions for a wide range of membrane
536 tension values.

537

538 **Discussion**

539 Since their first description in 1953, research over the years has revealed a variety of
540 roles for caveolae and/or caveolins in preserving biological functions [reviewed in [1,2]. Although caveolae were proposed to be involved in mechanoprotection and in
542 maintaining cellular integrity as early as the mid-1970's [84-86], it was not until our seminal
543 discovery that caveolae sense and respond to mechanical stress that the field was
544 prompted to reassess their classical functions in the context of cell mechanics [2,42,49-51]. We initially hypothesized that caveolar proteins could be released upon the mechanical
546 disassembly of caveolae, thereby mediating the mechanical response of the cell [48]. We
547 could indeed demonstrate that elevated membrane tension triggers the translocation of
548 the ATPase EHD2 from the neck of caveolae to the nucleus, where it regulates gene
549 transcription [68]. Cavin1 is also released from the caveolar coat in response to hypo-
550 osmotic shock [42,67,87]. Additionally, cavin3 can interact with BRCA1 and regulate multiple
551 cancer related pathways upon its release from caveolae that have been disassembled by
552 UV exposure or hypo-osmotic shock [88].

553 Our findings reveal that mechanical stress significantly augments the extent of Cav1
554 interaction with JAK1, PTEN, PTP1B, and eNOS. This observation, along with the
555 proposed role of non-caveolar Cav1 scaffolds in signaling [38], has led us to hypothesize
556 that the increased interaction may be attributed to the release of Cav1 molecules
557 originating from caveolae that have undergone mechanical disassembly. sptPALM

558 microscopy confirmed that the primary population of non-diffusive Cav1 particles, initially
559 constrained to confined domains under low membrane tension (likely within *bona fide*
560 caveolae), transitioned significantly as membrane tension progressively increased. This
561 transition was characterized by a diffusion pattern indicative of Cav1 scaffolds scattering
562 upon caveolae disassembly, accompanied by an increased population of freely diffusing
563 Cav1 particles and an increase in their diffusion coefficient. Additionally, in Cavin1$^{-/-}$ cells
564 where only non-caveolar Cav1 is present, we measured a diffusion coefficient for Cav1
565 particles that was strictly identical to the higher diffusion coefficient induced by hypo-
566 osmotic shock in WT cells. These observations confirm that the highly diffusive pool of
567 Cav1 molecules corresponds to non-caveolar Cav1. Similarly, we established a direct
568 correlation between the level of inhibition of STAT3 phosphorylation and the quantity of
569 non-caveolar Cav1.

570 These findings provide strong evidence for the role of non-caveolar Cav1 scaffolds
571 in the mechanical regulation of intracellular signaling. Since the expression of cavin
572 proteins seems limited to vertebrates, it has been proposed that caveolins can carry out
573 their functions independently of caveolae in most organisms. Likewise, various cell types
574 including neurons, lymphocytes, hepatocytes, and certain cancer cells do not express
575 cavins, suggesting that caveolins may exert caveola-independent functions in these cells
576 [72].

577 Early studies have reported the ability of Cav1 to interact with several effectors
578 through the Cav1-CSD domain [28,29,56,57]. Using CSD mimicking peptides and point
579 mutations in the Cav1-CSD, we provide unequivocal evidence of the CSD requirement
580 for the direct interaction between Cav1 and JAK1. Accordingly, it has been reported that

the deletion of the CSD abolished the inhibition of STAT3 phosphorylation caused by Cav1 overexpression [89]. It is remarkable that the CSD exhibits significant primary sequence similarities to the pseudo-substrate domain of SOCS1, which mediates JAK inhibition by SOCS1 [90,91]. In this context, it is interesting that another member of the SOCS family, SOCS3, relies on Cavin-1 for its localization at the plasma membrane in endothelial cells, and that STAT3 activation is increased when Cavin-1 is depleted [92]. It will be interesting to test if, under mechanical stress, SOCS3 may be released from Cavin-1, which would then compete with Cav1 scaffolds to bind to JAK1.

It has been proposed that the Cav1-CSD can recognize an aromatic-rich consensus sequence known as the caveolin binding motif (CBM), which is present in associated proteins [60,61]. However, *in silico* studies have raised doubts about the CSD-mediated interaction between Cav1 and CBM-containing proteins [93,94]. The potential formation of the JAK1-Cav1 complex was evaluated through computational protein-protein docking techniques, and we successfully identified a possible complex configuration that aligns with all experimental data. In particular, the involvement of the JH1 catalytic kinase domain of JAK1, marked by the highly accessible residue Y1059, is crucial. In the presence of Cav1, this residue is close to Cav-1 residues T90, V94, and W98, which, as demonstrated by targeted mutagenesis, are essential for establishing the Cav1-JAK1 complex. These residues are required for the functionality of the Cav1-CSD motif, and the docking experiments therefore further confirm the role of the Cav1-CSD in binding to JAK1.

Super-resolution imaging and network analysis have revealed the existence of different subclasses of Cav1 scaffolds, which serve as building blocks of *bona fide*

caveolae [40]. Similar analysis of our SMLM data from cells exposed to hypo-osmotic shock or subjected to cyclic stretch provided insights into the mechanical disassembly of caveolae into Cav1 scaffolds. This disassembly was strongly correlated with a significant increase in both Cav1 diffusion and its interaction with signaling effectors. The functionality of the Cav1-CSD has been debated, as it has been proposed, based on Cav1 sequence alignment, that Cav1-CSD is a hydrophobic motif embedded in the lipids of the plasma membrane, thus preventing direct physical interactions with cytosolic proteins [93,94]. Supporting this, a cell-free caveola reconstitution system based on *Leishmania tarentolae* extracts, aimed at mimicking native membrane insertion of Cav1, confirmed the key role of the Cav1-CSD physical accessibility for its interaction with cytosolic signaling molecules [95]. The preferential interaction of Cav1 scaffolds, as opposed to caveolae, with signaling molecules during periods of mechanical stress provides a potential explanation for the involvement of the Cav1-CSD. Indeed, recent structural data obtained on the minimal 8S Cav1 building block complex have revealed that the CSD is positioned at the outer rim of the 8S discoid complex [17]. Therefore, we can speculate that when caveolae are mechanically disassembled into scaffolds, along with subsequent lipid reorganization [96], the CSD, which may not be readily accessible within budded caveolae, could potentially be exposed and become available for binding to cytosolic proteins. In this context, the recent structural characterization of the Cav1 8S complex by cryo-EM has offered new insights into this interaction [97,98]. A recent study by Doktorova and colleagues utilized the structure of the Cav1 8S complex to perform coarse-grain molecular dynamics simulations of a single Cav1 8S embedded in lipid membranes of varying compositions [99]. During the simulations, the Cav1 8S complex

localized to highly curved surfaces, leading to the exposure of several Cav1-CSD residues, including T90, V94, and W98, to the aqueous environment. These findings are particularly significant because residues T90, V94, and W98, which exhibit increased solvent accessibility during the simulation, were identified by docking calculations as interacting with Tyr 1059 of JAK1, which is located within the JH1 catalytic kinase domain of JAK1 (Figure 4). These data are consistent with a recent study suggesting that the S2 and S1B Cav1 scaffolds exhibit a more exposed CSD with the surrounding molecular environment [100]. In addition, the simultaneous release of cavins from the caveola bulb, induced by mechanical stress, may also contribute to the enhanced accessibility of Cav1-CSD.

Docking experiments and coarse-grain molecular dynamics provide additional support for our biochemical and super-resolution data, offering a compelling explanation for why individual Cav1 scaffolds, such as the 8S complex, demonstrate an enhanced propensity to interact with the JAK1 kinase following caveolae mechanical disassembly. Many inhibitors of JAK1 interact with the JH1domain, likely explaining the inactivation of JAK1 catalytic activity by Cav1 scaffolds [101].

JAK1 inhibition was observed even in the absence of stimulation with IFN-α, indicating that this regulatory process may be extended to other cytokines that activate JAK kinases. In the context of our previous study on IL-6/STAT3 signaling in human muscle cells, it is probable that the control exerted by caveolae mechanosensing on this signaling axis operates through the same mechanism [102]. It is intriguing that JAK1-dependent STAT3 activation was specifically targeted while leaving STAT1 activation unaffected. Interestingly, our data indicate that TYK2, the other kinase operating in the

IFN-α signaling complex, does not interact with Cav1. These findings further support the dichotomy between STAT3, which is known for its oncogenic properties, and STAT1, which is recognized as a tumor suppressor [103]. The molecular basis underlying this signal specificity warrants further investigation in various cancer cells lines.

Our findings unveil a novel mechanism through which caveolae exert remote control over the regulation of various signaling pathways. This control takes place beyond the boundaries of the caveolae structure and relies on a dynamic exchange between caveolae and Cav1 scaffolds. The balance between these two distinct populations of Cav1 assemblies is finely tuned by variations of membrane tension and enables precise modulation of signaling outputs. The proposed mechanism finds support in a theoretical model that considers the thermodynamics of caveolae formation under mechanical stress. The model suggests that as membrane tension increases, there is a transition from caveolar Cav1 to Cav1 scaffolds, accompanied by an enhanced affinity of Cav1 towards its effectors.

Cav1 has long been known to interact with numerous proteins, including signaling molecules and membrane receptors. However, the lack of compelling evidence for the localization of these proteins inside caveolae, along with data arguing for exclusion of bulk plasma membrane proteins [33], raises a puzzling question regarding how caveolae can effectively regulate signaling effectors that are not found into caveolae. This study presents a new mechanistic insight into the regulation of cell signaling through caveolae. The reversible conversion of caveolae into Cav1 scaffolds enables the remote control of signaling molecules localized outside of caveolae.

Mechanical forces can regulate diverse cellular functions by directly influencing protein interactions, such as reinforcing [104,105] or destabilizing interactions [42,106] and controlling enzymatic reactions [107]. Furthermore, mechanical deformations have been shown to uncover concealed or cryptic binding sites, as demonstrated for vinculin and talin [108], as well as cryptic phosphorylation [109] or proteolysis sites [110]. Thus, there is a consensus that external mechanical stresses are transmitted directly and rapidly to induce local protein deformation in mechano-sensitive structures like integrin adhesions, the cytoskeleton, or the nucleus [78,111-113]. Our findings reveal a new paradigm of mechano-transduction, challenging the notion that mechanical forces trigger immediate local effects or are rapidly transmitted through the cell via cytoskeletal elements or the membrane. Instead, we demonstrate that the conversion of *bona fide* caveolae into caveolin scaffolds generates mechanical messengers that diffuse at the plasma membrane. Cav1 scaffolds interact with signaling effectors at distant locations from the initial mechano-sensing caveolae, with a time delay. Caveolae remote mechanosignaling may also serve as a mechanism for integrating and facilitating crosstalk with other mechanosensitive structures, such as integrin adhesions and the cytoskeleton. Notably, integrin adhesion and Cav1 have been functionally interconnected [37,114,115] and share common cytoskeleton partners [116] and signaling pathways [117-119]. In addition, caveolae have been associated with actin stress fibers and implicated in the regulation of their contractility [31,120,121]. In this context, it is interesting that protein deformation within integrin adhesion is not directly triggered by the transmission of external stretch but mediated by a delayed acto-myosin remodeling process [81].

The pathophysiological implications of remote mechanosignaling by caveolae remain to be investigated. Several of the signaling effectors regulated by this process, including PTEN, PTP1B, and STAT3, are well-known for their involvement in the control of tumorigenesis. The role of Cav1 and caveolae in cancer has sparked prolonged debates due to their seemingly contradictory behavior, with reports indicating both oncogenic and tumor suppressor properties [24,122-124]. This novel functional aspect of caveolae mechanics could have a substantial impact on tumor growth. The mechanical forces experienced by cancer cells throughout tumor progression may disrupt caveolae mechanosensing, thereby impairing the precise regulation of caveolae-mediated mechanosignaling.

Taken together, our findings represent a significant breakthrough in the field of intracellular signaling, revealing caveolae as crucial mechano-signaling devices capable of remotely fine-tuning specific signal transduction processes originating from the plasma membrane. This novel understanding of caveolae not only contributes to our comprehension of their functions but also holds profound implications for human pathophysiology.

Acknowledgements

We are grateful to Dr. Anne Kenworthy, Dr. Bing Han, and Dr. Milka Doktorova for sharing their data on coarse-grain molecular dynamics [99] and for their stimulating discussions. The core facilities and the CurieCoreTech recombinant antibodies platform of Institut Curie, the scientific and technical assistance from staff of the Cell and Tissue Imaging

(PICT-IBiSA) and the Nikon Imaging Centre at Institut Curie, member of the French National Research Infractucture France-BioImaging (ANR10-INBS-04) are acknowledged. We would like to thank C. Schietroma from Abbelight for technical assistance with SMLM (STORM) experiments. The help of the following people for providing materials or expertise is acknowledged: Dr. Radu. V. Stan (Dartmouth College, USA), and Dr. Miguel Del Pozo (Spanish National Centre for Cardiovascular research, Spain). This work was supported by institutional grants from the Curie Institute, Institut National de la Sante et de la Recherche Medicale, CNRS, and by specific grants from Agence Nationale de la Recherche (ANR-19-CE15-0020-02 to C.L.) and INCa 2018-1-PL BIO-08-ICR-1 (Decision N° 2018-154). Funding from France Canada Research Fund: NVKA GR013361 - FCRF to C.L. and I.R.N. is acknowledged. G.G. was supported by the INCA (AAP PLBIO no. 2020-109), the ANR (ANR-21-CE11-0004-01), the French government in the framework of the University of Bordeaux's IdEx "Investments for the Future" program / GPR BRAIN_2030, GPR LIGHT. O.R. was supported by the ANR (ANR-20-CE42-0003-02) and the Nouvelle-Aquitaine Regional Council (AAPR2021-2020-12041310). S.K.M was supported by a PhD fellowship from Ligue Nationale contre le Cancer, N.T. by a PhD fellowship from Ministère de l'Enseignement Supérieur et de la Recherche and M.D. by a PhD fellowship from Association Française contre les Myopathies (AFM): CAV-MUT (17151). The Lamaze and Sens teams are members of Labex Cell(n)scale ANR-10-LBX-0038, part of the IDEX PSL ANR-10-IDEX-0001-02. I. S. M. was supported by the European Regional Development Fund through the COMPETE 2020–Operational Programme for Competitiveness and Internationalization and Portuguese National Funds via Fundação para a Ciência e a Tecnologia (FCT)

[LA/P/0058/2020, UIDB/04539/2020, UIDP/04539/2020, and DSAIPA/DS/0118/2020, http://doi.org/10.54499/DSAIPA/DS/0118/2020). The funders had no role in study design, data collection and analysis, decision to publish or preparation of the manuscript.

Author contributions statement

S.K.M., N.T., I.S.M, and C.M.B designed and performed the experiments, analyzed and interpreted the data, and wrote the manuscript. O.R. designed and performed the spt-PALM experiments, analyzed and interpreted the corresponding data. X.Z., F.N.V. and G.G. designed and performed the DNA-PAINT experiments. A.R., C.G., P.G.T., R.R. and M.D. performed experiments. I.B. performed RPPA analysis. I.K., I.R.N. and G.H. analyzed and interpreted the 3D STORM data using 3D SMLM network analysis. P.S. designed the physical model for theoretical validation of the study. G.G., O.R., I.K., I.R.N. and P.S. proofread and edited the manuscript. C.L. supervised the study, designed the experiments, interpreted the data, and wrote the manuscript. All authors discussed the results and commented on the manuscript.

Ethics declarations

Competing interests

The authors declare no competing interests.

Figure Legends

Figure 1: High throughput screening of signaling pathways modulated by caveolae mechanics. (A) Heat map of activation of signaling effectors in MLEC WT and MLEC Cav1$^{-/-}$ cells treated or not with Type-I IFN under conditions of resting or uniaxial stretch. **(B)** p44/42 MAPK, AKT and PKCα phosphorylation levels under conditions of resting or uniaxial stretch in MLEC WT and CAV1$^{-/-}$ cells. **(C, D)** STAT1 and STAT3 phosphorylation levels upon **(C)** Type-I IFN stimulation and **(D)** uniaxial stretch in MLEC WT and CAV1$^{-/-}$ cells. **(E)** STAT3 phosphorylation levels induced by IFN-α stimulation in MLEC WT (left panel) and CAV1$^{-/-}$ (right panel) cells subjected to uniaxial stretch or not. Representative immunoblots and quantification of signal ratio relative to "CTRL" condition for N=3 independent experiments; mean values ± SEM. **(F)** Immunofluorescence images of nuclear translocation of pSTAT1 and pSTAT3 in MLEC WT (top) and MLEC Cav1$^{-/-}$ (bottom) cells subjected to uniaxial stretch or not. Representative data for N=3 independent experiments. Statistics were performed using two tailed unpaired t-test; *P<0.05 and ns: not significant.

Figure 2: Cav1 dependent inhibition of STAT3 activation is mediated through JAK1 interaction. (A) Co-immunoprecipitation of endogenous Cav1 and JAK1 in iso-osmotic (ISO), hypo-osmotic (HYPO) and successive hypo-osmotic and iso-osmotic treatment (REC) in MLEC WT cells. Quantification is based on the signal intensity ratio (JAK1 and Cav1) relative to the intensity of the corresponding immuno-precipitated protein (Cav1 and JAK1 respectively). **(B)** Co-immunoprecipitation of endogenous JAK1 with Cav1 and corresponding Tyr705 pSTAT3 levels in MLEC WT cells upon IFN-α stimulation in ISO, HYPO and REC conditions. Quantification for JAK1 is based on the signal intensity ratio of JAK1 relative to the intensity of immuno-precipitated Cav1 while quantification for Tyr705 pSTAT3 is based on the signal intensity ratio of Tyr705 pSTAT3 relative to the intensity of total protein obtained from strain-free blot. The corresponding representative stain-free blot is shown. **(C)** Co-immunoprecipitation of endogenous eNOS and PTP1B with Cav1 in MLEC WT cells under ISO, HYPO and REC conditions. Quantifications of eNOS and PTP1B signals are based on the signal intensity ratio relative to the immunoprecipitated Cav1 protein levels. **(D)** Co-immunoprecipitation of endogenous PTEN with Cav1 and corresponding Ser473 pAKT levels in MLEC WT cells under ISO, HYPO and REC conditions. Quantification for PTEN is based on the signal intensity ratio of PTEN relative to the intensity of immuno-precipitated Cav1 while quantification for Ser473 pAKT is based on the signal intensity ratio of Ser473 pAKT relative to the intensity of total protein obtained from strain-free blot. The corresponding representative stain-free blot is shown. All panels exhibit representative immunoblots for N=3 independent experiments. Data shown are mean values ± SEM. Statistics were performed using

repeated measures multiple-comparison one-way ANOVA. *P<0.05; **P<0.01; ***P<0.001; ****P<0.0001 and ns: not significant.

Figure 3: Cav1-JAK1 interaction requires the caveolin scaffolding domain. (A) Representative immunoblot of RFP-trap pull-down performed on MLEC CAV1$^{-/-}$ cells expressing either Cav1(WT)-RFP or Cav1(F92A/V94A)-RFP or RFP (left). Quantification of JAK1/Cav1 signal ratio relative to "Cav1-RFP WT " condition (right); Data shown are N=3 independent experiments. **(B)** Representative wide field immunofluorescence images of nuclear translocation of Tyr705 pSTAT3 (green) in IFN-α stimulated MLEC CAV1$^{-/-}$ cells expressing either exogenous Cav1(WT)-RFP or Cav1(F92A/V94A)-RFP (red). Quantification of nuclear/cytosol Tyr 705 pSTAT3 signal ratio in cells positive for: Control (N=49), Cav1(WT)-RFP (N=72) and Cav1(F92A/V94A)-RFP (N=38), pooled from N=3 independent experiments. **(C)** Representative immunoblots of levels of Tyr705 pSTAT3 upon IFN-α stimulation in MLEC WT cells treated with either control peptide and CavTratin (right) or control peptide and CavNoxin (left). Data shown are N=6 (CavTratin) and N=9 (CavNoxin) independent experiments. **(D)** In-vitro ADP production via ATP conversion by recombinant JAK1 relative to peptide log concentration (μM). For **(A-D)** data shown are mean values ± SEM. Statistics for **(A, B)** were processed using standard multiple-comparison one-way ANOVA and for **(C)** using two-tailed unpaired t-test; *P<0.05; **P<0.01; ****P<0.0001 and ns: not significant.

Figure 4: Cav1/JAK1 Complex as inferred by computational modeling and docking guided by experimental-derived restraints. JAK1 is depicted in smudge and Cav1 in dirty violet. **(A)** Side view (left) and bottom view (right). **(B)** Zoom on key residues of the JAK1 region that engage directly with residues from the Cav1 CSD. These critical interacting residues were highlighted using stick representations for clarity.

Figure 5: Upon osmotic shock, Cav1 is released from caveolae and undergoes lateral free diffusion along the plasma membrane. (A) Top: Super-resolution PALM intensity images of mEos3.2-Cav1 in MLEC WT cells in isotonic (ISO) medium (left) and during hypotonic (HYPO) shock (right) obtained from a sptPALM sequence (50 Hz, >80 s). Inset: low resolution image of Cav1-GFP, which was co-expressed for caveolae labelling (scale bar: 3 µm). Bottom: corresponding color-coded trajectories of Cav1 in the same cell showing the various diffusion modes: free diffusion (blue), confined diffusion (green) and immobilization (red). **(B)** Distribution of the diffusion coefficient D computed from the trajectories of mEos3.2-Cav1 in MLEC WT cells in ISO (black) and HYPO (blue) conditions, shown in a logarithmic scale. The grey area including D values inferior to 0.011 $\mu m^2.s\text{-}1$ corresponds to immobilized proteins. Data shown are mean values ± SEM. Box plots displaying the median (notch) and mean (square) ± percentile (25–75%) of diffusion coefficients corresponding to the free diffusive trajectories of mEos3.2-Cav1 in MLEC WT cells under ISO and HYPO conditions. Fraction of mEos3.2-Cav1 undergoing free diffusion, confined diffusion or immobilization in MLEC WT cells under ISO and HYPO conditions. **(C and D)** Distribution of the diffusion coefficient D computed from the trajectories of mEos3.2-Cav1 in MLEC WT cells subjected to HYPO condition between t=0 mins to t=10 mins **(C)** and in MLEC WT cells initially at HYPO condition which are subsequently subjected to REC condition between t=1 min to t=30 mins **(D)**. **(E)** Super-resolution PALM intensity images of mEos3.2-Cav1 in MEF Cavin1$^{-/-}$ cells (left) and MEF Cavin1$^{-/-}$ cells rescued with transfected Cavin1-mEGFP (right) obtained from a sptPALM sequence (50 Hz, >80 s). Inset: low resolution image of mEos3.2-Cav1 (left) and Cavin1-mEGFP (right), for caveolae labelling (scale bar: 3 µm). Corresponding color-coded

853 trajectories of caveolin-1 in the same cell showing the various diffusion modes: free
854 diffusion (blue), confined diffusion (green) and immobilization (red). **(F)** Distribution of the
855 diffusion coefficient D computed from the trajectories of mEos3.2-Cav1 in MEF WT cells
856 in ISO (black) and HYPO (blue) conditions, shown in a logarithmic scale. The grey area
857 including D values inferior to 0.011 µm².s-1 corresponds to immobilized proteins. Data
858 shown are mean values ± SEM. **(G)** Trajectories of mEos3.2-Cav1 in MEF Cavin1$^{-/-}$ cells
859 (blue) and MEF Cavin1$^{-/-}$ cells rescued with transfected Cavin1-mEGFP (green). **(H)** Box
860 plots displaying the median (notch) and mean (square) ± percentile (25–75%) of diffusion
861 coefficients corresponding to the free diffusive trajectories of mEos3.2-Cav1 in MEF WT
862 cells under ISO and HYPO conditions and in MEF Cavin1$^{-/-}$ cells transfected or not with
863 Cavin1-mEGFP. Fraction of mEos3.2-Cav1 undergoing free diffusion, confined diffusion
864 or immobilization in MEF WT cells under ISO and HYPO conditions and in MEF Cavin1$^{-/-}$
865 cells transfected or not with Cavin1-mEGFP. **(I)** Immunoblots for STAT3 phosphorylation
866 levels in MEF Cavin1$^{-/-}$ cells (NT) and MEF Cavin1$^{-/-}$ cells transfected with Cavin1-mEGFP
867 (Cavin1-mEGFP) at steady state (left) or upon IFN-α stimulation (right). **(J)** Representative
868 immunoblots of IFN-α induced STAT3 phosphorylation levels in MEF Cavin1$^{-/-}$ cells
869 expressing either low, medium or high levels of Caveolin-1 and quantification of signal
870 ratio relative to the "low" condition. In **(A-H)**, data shown for mEos3.2-Cav1 diffusions in
871 MLEC cells (ISO, n=9; HYPO, n=10), MEF WT cells (ISO, n=8; HYPO, n=8), in MEF
872 Cavin1-/- cells rescued with transfected Cavin1-mEGFP (ISO, n=11) and MEF Cavin1-/-
873 cells (ISO, n=9) are pooled from N=2 independent experiments. Statistical significance
874 was obtained for **(A-H)** using two-tailed, non-parametric Mann–Whitney rank sum test and

for **(J)** using multiple-comparison ANOVA. ****P<0.0001, ***P<0.001, **P<0.01, *P<0.05 and ns, not significant.

Figure 6: Nanoscale visualization of Cav1 and its fate in response to mechanical stress. (A) Representative 2D single-color dSTORM image of a MLEC WT cell stained for Cav1. Inset is higher magnification. **(B)** A comparison of representative raw 2D STORM image vs processed image to showcase the reliability and integrity of the 3D SMLM network analysis used to classify Cav1 clusters as caveolae and non-caveolar Cav1 scaffolds (S2, S1B and S1A). **(C)** Quantification per unit area of number of caveolae and the three subclasses of non-caveolar Cav1 scaffolds from post-cluster segmentation images of MLEC WT cells in ISO (n=30) and HYPO (n=30) conditions imaged using 3D dSTORM. Data shown are mean values ± SEM pooled from ROIs from N= 3 independent experiments (15 cells each for ISO and HYPO). **(D)** DNA-PAINT images (top) of Caveolin-1 in MLEC Cav1$^{-/-}$ cells re-transfected with Cav1-GFP at steady state (CTRL) and under conditions of cyclic stretch (30% strain, 0.5Hz for 30 min) on a PDMS stretching device (Stretch). Images show first-rank order density maps (middle) from SR-Tesseler, normalized by the average localization density. The corresponding detected clusters are show in bottom panel, highlighted with colors. The area outlined in the left panel is shown at a higher magnification in the right panel for the respective conditions. Cluster size distribution of Caveolin-1 in cells without (orange) or with (magenta) cyclic stretch. Bold lines represent mean values of n_{CTRL}=1929 and $n_{Stretch}$=3531 clusters pooled from N=3 independent experiments. Fraction of clusters of Caveolin-1 below 70 nm (dashed) and above 70 nm (smooth) in cells without (orange) or with (magenta) cyclic stretch. Data shown are mean values ± SEM. **(E)** Representative 3D STORM image of localizations of JAK1 and the various Cav1 populations superimposed with the JAK1 localizations within a defined ROI under iso-osmotic (top) and hypo-osmotic shock (bottom) conditions. The

902 objects generated for clusters of JAK1 and Cav1 along with the extracted centroids for the
903 corresponding pairs of objects are also depicted. Data shown are mean values ± SEM
904 from ROIs in ISO (n=15 cells) and HYPO (n= 15 cells) pooled from N= 3 independent
905 experiments for the different Cav1 populations. For **(C)** statistics were performed using
906 two tailed unpaired t-test and for **(E)** using repeated measures multiple-comparison
907 ANOVA. ***P<0.001, **P<0.01.

908

909

Figure 7: Physical model of caveolae formation under stress. (A) Different Cav1 and membrane-associated signaling effectors included in the physical model (free S1 oligomers, full caveolae, hemispherical S2 domains, active effectors, and complexes of Cav1 and inactive effectors). Sketch of the model (right). **(B)** Variation of the three Cav1 populations with membrane tension (the blue line represents the sum of all diffusing Cav1 states). **(C)** Variation of the fraction of active and inactive effectors with membrane tension. Solid lines are within the tension range explored in stretching experiments (data points in B are from Figure 5E) and dashed lines are theoretical extrapolation over a broader range of tension variation. Parameters: $e_b=3.6$, $\lambda=1.76$, $\rho_{tot}=0.33$, $\varepsilon=2.6$, $\rho_{(j,tot)}=0.02$.

References

1. Lamaze, C., Tardif, N., Dewulf, M., Vassilopoulos, S., and Blouin, C.M. (2017). The caveolae dress code: structure and signaling. Curr Opin Cell Biol *47*, 117-125. 10.1016/j.ceb.2017.02.014.
2. Parton, R.G., Del Pozo, M.A., Vassilopoulos, S., Nabi, I.R., Le Lay, S., Lundmark, R., Kenworthy, A.K., Camus, A., Blouin, C.M., Sessa, W.C., and Lamaze, C. (2020). Caveolae: The FAQs. Traffic *21*, 181-185. 10.1111/tra.12689.
3. Palade, G.E. (1953). The fine structure of blood capillaries. J. Appl. Phys. *24*, 1424.
4. Yamada, E. (1955). The fine structure of the gall bladder epithelium of the mouse. J Biophys Biochem Cytol *1*, 445-458.
5. Rothberg, K.G., Heuser, J.E., Donzell, W.C., Ying, Y.S., Glenney, J.R., and Anderson, R.G. (1992). Caveolin, a protein component of caveolae membrane coats. Cell *68*, 673-682.
6. Way, M., and Parton, R.G. (1996). M-caveolin, a muscle-specific caveolin-related protein. FEBS Lett *378*, 108-112.
7. Scherer, P.E., Okamoto, T., Chun, M., Nishimoto, I., Lodish, H.F., and Lisanti, M.P. (1996). Identification, sequence, and expression of caveolin-2 defines a caveolin gene family. Proc Natl Acad Sci U S A *93*, 131-135.
8. Aboulaich, N., Vainonen, J.P., Stralfors, P., and Vener, A.V. (2004). Vectorial proteomics reveal targeting, phosphorylation and specific fragmentation of polymerase I and transcript release factor (PTRF) at the surface of caveolae in human adipocytes. Biochem J *383*, 237-248.
9. Hill, M.M., Bastiani, M., Luetterforst, R., Kirkham, M., Kirkham, A., Nixon, S.J., Walser, P., Abankwa, D., Oorschot, V.M., Martin, S., et al. (2008). PTRF-Cavin, a conserved cytoplasmic protein required for caveola formation and function. Cell *132*, 113-124.
10. Liu, L., and Pilch, P.F. (2008). A critical role of cavin (polymerase I and transcript release factor) in caveolae formation and organization. J Biol Chem *283*, 4314-4322.
11. Bastiani, M., Liu, L., Hill, M.M., Jedrychowski, M.P., Nixon, S.J., Lo, H.P., Abankwa, D., Luetterforst, R., Fernandez-Rojo, M., Breen, M.R., et al. (2009). MURC/Cavin-4 and cavin family members form tissue-specific caveolar complexes. J Cell Biol *185*, 1259-1273.
12. Sverdlov, M., Shinin, V., Place, A.T., Castellon, M., and Minshall, R.D. (2009). Filamin A regulates caveolae internalization and trafficking in endothelial cells. Mol Biol Cell *20*, 4531-4540. 10.1091/mbc.e08-10-0997.
13. Senju, Y., Itoh, Y., Takano, K., Hamada, S., and Suetsugu, S. (2011). Essential role of PACSIN2/syndapin-II in caveolae membrane sculpting. J Cell Sci *124*, 2032-2040.
14. Hansen, C.G., Howard, G., and Nichols, B.J. (2011). Pacsin 2 is recruited to caveolae and functions in caveolar biogenesis. J Cell Sci *124*, 2777-2785.
15. Moren, B., Shah, C., Howes, M.T., Schieber, N.L., McMahon, H.T., Parton, R.G., Daumke, O., and Lundmark, R. (2012). EHD2 regulates caveolar dynamics via ATP-driven targeting and oligomerization. Mol Biol Cell *23*, 1316-1329.
16. Koch, D., Westermann, M., Kessels, M.M., and Qualmann, B. (2012). Ultrastructural freeze-fracture immunolabeling identifies plasma membrane-localized syndapin II as a crucial factor in shaping caveolae. Histochem Cell Biol *138*, 215-230. 10.1007/s00418-012-0945-0.
17. Porta, J.C., Han, B., Gulsevin, A., Chung, J.M., Peskova, Y., Connolly, S., McHaourab, H.S., Meiler, J., Karakas, E., Kenworthy, A.K., and Ohi, M.D. (2022). Molecular architecture of the human caveolin-1 complex. Sci Adv *8*, eabn7232. 10.1126/sciadv.abn7232.

18. Patel, H.H., Murray, F., and Insel, P.A. (2008). Caveolae as organizers of pharmacologically relevant signal transduction molecules. Annu Rev Pharmacol Toxicol *48*, 359-391.
19. Lajoie, P., and Nabi, I.R. (2010). Lipid rafts, caveolae, and their endocytosis. International review of cell and molecular biology *282*, 135-163. 10.1016/s1937-6448(10)82003-9.
20. Pilch, P.F., Meshulam, T., Ding, S., and Liu, L. (2011). Caveolae and lipid trafficking in adipocytes. Clin Lipidol *6*, 49-58.
21. Parton, R.G., McMahon, K.A., and Wu, Y. (2020). Caveolae: Formation, dynamics, and function. Curr Opin Cell Biol *65*, 8-16. 10.1016/j.ceb.2020.02.001.
22. Minshall, R.D., Sessa, W.C., Stan, R.V., Anderson, R.G., and Malik, A.B. (2003). Caveolin regulation of endothelial function. Am J Physiol Lung Cell Mol Physiol *285*, L1179-1183. 10.1152/ajplung.00242.2003.
23. Williams, J.J., and Palmer, T.M. (2014). Cavin-1: caveolae-dependent signalling and cardiovascular disease. Biochem Soc Trans *42*, 284-288. 10.1042/bst20130270.
24. Singh, V., and Lamaze, C. (2020). Membrane tension buffering by caveolae: a role in cancer? Cancer metastasis reviews *2*, 505-517. 10.1007/s10555-020-09899-2.
25. Liu, L. (2020). Lessons from cavin-1 deficiency. Biochem Soc Trans *48*, 147-154. 10.1042/bst20190380.
26. Boscher, C., and Nabi, I.R. (2012). Caveolin-1: role in cell signaling. Advances in experimental medicine and biology *729*, 29-50. 10.1007/978-1-4614-1222-9_3.
27. Fridolfsson, H.N., Roth, D.M., Insel, P.A., and Patel, H.H. (2014). Regulation of intracellular signaling and function by caveolin. Faseb j *28*, 3823-3831. 10.1096/fj.14-252320.
28. Couet, J., Sargiacomo, M., and Lisanti, M.P. (1997). Interaction of a receptor tyrosine kinase, EGF-R, with caveolins. Caveolin binding negatively regulates tyrosine and serine/threonine kinase activities. J Biol Chem *272*, 30429-30438. 10.1074/jbc.272.48.30429.
29. Nystrom, F.H., Chen, H., Cong, L.N., Li, Y., and Quon, M.J. (1999). Caveolin-1 interacts with the insulin receptor and can differentially modulate insulin signaling in transfected Cos-7 cells and rat adipose cells. Mol Endocrinol *13*, 2013-2024. 10.1210/mend.13.12.0392.
30. Bernatchez, P.N., Bauer, P.M., Yu, J., Prendergast, J.S., He, P., and Sessa, W.C. (2005). Dissecting the molecular control of endothelial NO synthase by caveolin-1 using cell-permeable peptides. Proc Natl Acad Sci U S A *102*, 761-766.
31. Grande-Garcia, A., Echarri, A., de Rooij, J., Alderson, N.B., Waterman-Storer, C.M., Valdivielso, J.M., and del Pozo, M.A. (2007). Caveolin-1 regulates cell polarization and directional migration through Src kinase and Rho GTPases. J Cell Biol *177*, 683-694. 10.1083/jcb.200701006.
32. Ariotti, N., Fernandez-Rojo, M.A., Zhou, Y., Hill, M.M., Rodkey, T.L., Inder, K.L., Tanner, L.B., Wenk, M.R., Hancock, J.F., and Parton, R.G. (2014). Caveolae regulate the nanoscale organization of the plasma membrane to remotely control Ras signaling. J Cell Biol *204*, 777-792. 10.1083/jcb.201307055.
33. Shvets, E., Bitsikas, V., Howard, G., Hansen, C.G., and Nichols, B.J. (2015). Dynamic caveolae exclude bulk membrane proteins and are required for sorting of excess glycosphingolipids. Nature communications *6*, 6867. 10.1038/ncomms7867.
34. Lajoie, P., Partridge, E.A., Guay, G., Goetz, J.G., Pawling, J., Lagana, A., Joshi, B., Dennis, J.W., and Nabi, I.R. (2007). Plasma membrane domain organization regulates EGFR signaling in tumor cells. J Cell Biol *179*, 341-356.
35. Joshi, B., Strugnell, S.S., Goetz, J.G., Kojic, L.D., Cox, M.E., Griffith, O.L., Chan, S.K., Jones, S.J., Leung, S.P., Masoudi, H., et al. (2008). Phosphorylated caveolin-1 regulates

Rho/ROCK-dependent focal adhesion dynamics and tumor cell migration and invasion. Cancer Res *68*, 8210-8220. 10.1158/0008-5472.Can-08-0343.

36. Moon, H., Lee, C.S., Inder, K.L., Sharma, S., Choi, E., Black, D.M., KA, L.C., Winterford, C., Coward, J.I., Ling, M.T., et al. (2014). PTRF/cavin-1 neutralizes non-caveolar caveolin-1 microdomains in prostate cancer. Oncogene *33*, 3561-3570. 10.1038/onc.2013.315.
37. Meng, F., Saxena, S., Liu, Y., Joshi, B., Wong, T.H., Shankar, J., Foster, L.J., Bernatchez, P., and Nabi, I.R. (2017). The phospho-caveolin-1 scaffolding domain dampens force fluctuations in focal adhesions and promotes cancer cell migration. Mol Biol Cell *28*, 2190-2201. 10.1091/mbc.E17-05-0278.
38. Lajoie, P., Goetz, J.G., Dennis, J.W., and Nabi, I.R. (2009). Lattices, rafts, and scaffolds: domain regulation of receptor signaling at the plasma membrane. J Cell Biol *185*, 381-385.
39. Khater, I.M., Meng, F., Wong, T.H., Nabi, I.R., and Hamarneh, G. (2018). Super Resolution Network Analysis Defines the Molecular Architecture of Caveolae and Caveolin-1 Scaffolds. Scientific reports *8*, 9009. 10.1038/s41598-018-27216-4.
40. Khater, I.M., Liu, Q., Chou, K.C., Hamarneh, G., and Nabi, I.R. (2019). Super-resolution modularity analysis shows polyhedral caveolin-1 oligomers combine to form scaffolds and caveolae. Scientific reports *9*, 9888. 10.1038/s41598-019-46174-z.
41. Lolo, F.N., Walani, N., Seemann, E., Zalvidea, D., Pavón, D.M., Cojoc, G., Zamai, M., Viaris de Lesegno, C., Martínez de Benito, F., Sánchez-Álvarez, M., et al. (2022). Caveolin-1 dolines form a distinct and rapid caveolae-independent mechanoadaptation system. Nat Cell Biol *25*. 10.1038/s41556-022-01034-3.
42. Sinha, B., Koster, D., Ruez, R., Gonnord, P., Bastiani, M., Abankwa, D., Stan, R.V., Butler-Browne, G., Vedie, B., Johannes, L., et al. (2011). Cells respond to mechanical stress by rapid disassembly of caveolae. Cell *144*, 402-413.
Comment by Mayor, S., 2011, Cell 2144(2013): 2323-2324. 10.1016/j.cell.2010.12.031.
43. Cheng, J.P., Mendoza-Topaz, C., Howard, G., Chadwick, J., Shvets, E., Cowburn, A.S., Dunmore, B.J., Crosby, A., Morrell, N.W., and Nichols, B.J. (2015). Caveolae protect endothelial cells from membrane rupture during increased cardiac output. J Cell Biol *211*, 53-61. 10.1083/jcb.201504042.
44. Lo, H.P., Nixon, S.J., Hall, T.E., Cowling, B.S., Ferguson, C., Morgan, G.P., Schieber, N.L., Fernandez-Rojo, M.A., Bastiani, M., Floetenmeyer, M., et al. (2015). The caveolin-cavin system plays a conserved and critical role in mechanoprotection of skeletal muscle. J Cell Biol *210*, 833-849. 10.1083/jcb.201501046.
45. Elliott, M.H., Ashpole, N.E., Gu, X., Herrnberger, L., McClellan, M.E., Griffith, G.L., Reagan, A.M., Boyce, T.M., Tanito, M., Tamm, E.R., and Stamer, W.D. (2016). Caveolin-1 modulates intraocular pressure: implications for caveolae mechanoprotection in glaucoma. Scientific reports *6*, 37127. 10.1038/srep37127.
46. Lim, Y.W., Lo, H.P., Ferguson, C., Martel, N., Giacomotto, J., Gomez, G.A., Yap, A.S., Hall, T.E., and Parton, R.G. (2017). Caveolae Protect Notochord Cells against Catastrophic Mechanical Failure during Development. Curr Biol *27*, 1968-1981.e1967. 10.1016/j.cub.2017.05.067.
47. Garcia, J., Bagwell, J., Njaine, B., Norman, J., Levic, D.S., Wopat, S., Miller, S.E., Liu, X., Locasale, J.W., Stainier, D.Y.R., and Bagnat, M. (2017). Sheath Cell Invasion and Trans-differentiation Repair Mechanical Damage Caused by Loss of Caveolae in the Zebrafish Notochord. Curr Biol *27*, 1982-1989.e1983. 10.1016/j.cub.2017.05.035.
48. Nassoy, P., and Lamaze, C. (2012). Stressing caveolae new role in cell mechanics. Trends Cell Biol *22*, 381-389. S0962-8924(12)00074-8 [pii]. 10.1016/j.tcb.2012.04.007 [doi].
49. Parton, R.G., and Del Pozo, M.A. (2013). Caveolae as plasma membrane sensors, protectors and organizers. Nat Rev Mol Cell Biol *14*, 98-112.

50. Cheng, J.P., and Nichols, B.J. (2016). Caveolae: One Function or Many? Trends Cell Biol *26*, 177-189. 10.1016/j.tcb.2015.10.010.
51. Del Pozo, M.A., Lolo, F.N., and Echarri, A. (2021). Caveolae: Mechanosensing and mechanotransduction devices linking membrane trafficking to mechanoadaptation. Curr Opin Cell Biol *68*, 113-123. 10.1016/j.ceb.2020.10.008.
52. Boellner, S., and Becker, K.F. (2015). Reverse Phase Protein Arrays-Quantitative Assessment of Multiple Biomarkers in Biopsies for Clinical Use. Microarrays (Basel) *4*, 98-114. 10.3390/microarrays4020098.
53. Schreiber, G., and Piehler, J. (2015). The molecular basis for functional plasticity in type I interferon signaling. Trends in immunology *36*, 139-149. 10.1016/j.it.2015.01.002.
54. Geletu, M., Taha, Z., Arulanandam, R., Mohan, R., Assi, H.H., Castro, M.G., Nabi, I.R., Gunning, P.T., and Raptis, L.P. (2019). Effect of Caveolin-1 upon Stat3-ptyr705 levels in breast and lung carcinoma cells. Biochemistry and cell biology = Biochimie et biologie cellulaire. 10.1139/bcb-2018-0367.
55. Geletu, M., Mohan, R., Arulanandam, R., Berger-Becvar, A., Nabi, I.R., Gunning, P.T., and Raptis, L. (2018). Reciprocal regulation of the Cadherin-11/Stat3 axis by caveolin-1 in mouse fibroblasts and lung carcinoma cells. Biochimica et biophysica acta. Molecular cell research *1865*, 794-802. 10.1016/j.bbamcr.2018.02.004.
56. Li, S., Couet, J., and Lisanti, M.P. (1996). Src tyrosine kinases, Galpha subunits, and H-Ras share a common membrane-anchored scaffolding protein, caveolin. Caveolin binding negatively regulates the auto-activation of Src tyrosine kinases. J Biol Chem *271*, 29182-29190.
57. García-Cardeña, G., Martasek, P., Masters, B.S., Skidd, P.M., Couet, J., Li, S., Lisanti, M.P., and Sessa, W.C. (1997). Dissecting the interaction between nitric oxide synthase (NOS) and caveolin. Functional significance of the nos caveolin binding domain in vivo. J Biol Chem *272*, 25437-25440. 10.1074/jbc.272.41.25437.
58. Bernatchez, P., Sharma, A., Bauer, P.M., Marin, E., and Sessa, W.C. (2011). A noninhibitory mutant of the caveolin-1 scaffolding domain enhances eNOS-derived NO synthesis and vasodilation in mice. J Clin Invest *121*, 3747-3755.
59. Hayer, A., Stoeber, M., Bissig, C., and Helenius, A. (2009). Biogenesis of Caveolae: Stepwise Assembly of Large Caveolin and Cavin Complexes. Traffic *3*, 3.
60. Couet, J., Li, S., Okamoto, T., Ikezu, T., and Lisanti, M.P. (1997). Identification of peptide and protein ligands for the caveolin-scaffolding domain. Implications for the interaction of caveolin with caveolae-associated proteins. J Biol Chem *272*, 6525-6533. 10.1074/jbc.272.10.6525.
61. Oka, N., Yamamoto, M., Schwencke, C., Kawabe, J., Ebina, T., Ohno, S., Couet, J., Lisanti, M.P., and Ishikawa, Y. (1997). Caveolin interaction with protein kinase C. Isoenzyme-dependent regulation of kinase activity by the caveolin scaffolding domain peptide. J Biol Chem *272*, 33416-33421. 10.1074/jbc.272.52.33416.
62. Rosário-Ferreira, N., Bonvin, A.M.J.J., and Moreira, I.S. (2022). Using machine-learning-driven approaches to boost hot-spot's knowledge. Computational Molecular Science *12*, e1602-e1606.
63. Lee, H., Xie, L., Luo, Y., Lee, S.Y., Lawrence, D.S., Wang, X.B., Sotgia, F., Lisanti, M.P., and Zhang, Z.Y. (2006). Identification of phosphocaveolin-1 as a novel protein tyrosine phosphatase 1B substrate. Biochemistry *45*, 234-240. 10.1021/bi051560j.
64. Caselli, A., Mazzinghi, B., Camici, G., Manao, G., and Ramponi, G. (2002). Some protein tyrosine phosphatases target in part to lipid rafts and interact with caveolin-1. Biochem Biophys Res Commun *296*, 692-697. 10.1016/s0006-291x(02)00928-2.
65. Lolo, F.-N., Pavón, D.M., Grande, A., Elósegui Artola, A., Segatori, V.I., Sánchez, S., Trepat, X., Roca-Cusachs, P., and del Pozo, M.A. (2022). Caveolae couple mechanical stress to integrin recycling and activation. eLife *11*, e82348. 10.7554/eLife.82348.

66. Monteiro, P., Remy, D., Lemerle, E., Routet, F., Macé, A.S., Guedj, C., Ladoux, B., Vassilopoulos, S., Lamaze, C., and Chavrier, P. (2023). A mechanosensitive caveolae-invadosome interplay drives matrix remodelling for cancer cell invasion. Nat Cell Biol *25*, 1787-1803. 10.1038/s41556-023-01272-z.
67. Gambin, Y., Ariotti, N., McMahon, K.A., Bastiani, M., Sierecki, E., Kovtun, O., Polinkovsky, M.E., Magenau, A., Jung, W., Okano, S., et al. (2013). Single-molecule analysis reveals self assembly and nanoscale segregation of two distinct cavin subcomplexes on caveolae. eLife *3*, e01434. 10.7554/eLife.01434.
68. Torrino, S., Shen, W.W., Blouin, C.M., Mani, S.K., Viaris de Lesegno, C., Bost, P., Grassart, A., Koster, D., Valades-Cruz, C.A., Chambon, V., et al. (2018). EHD2 is a mechanotransducer connecting caveolae dynamics with gene transcription. J Cell Biol *217*, 4092-4105. 10.1083/jcb.201801122.
69. Rossier, O., Octeau, V., Sibarita, J.B., Leduc, C., Tessier, B., Nair, D., Gatterdam, V., Destaing, O., Albiges-Rizo, C., Tampe, R., et al. (2012). Integrins beta1 and beta3 exhibit distinct dynamic nanoscale organizations inside focal adhesions. Nat Cell Biol *14*, 1057-1067. 10.1038/ncb2588.
70. Mehidi, A., Kage, F., Karatas, Z., Cercy, M., Schaks, M., Polesskaya, A., Sainlos, M., Gautreau, A.M., Rossier, O., Rottner, K., and Giannone, G. (2021). Forces generated by lamellipodial actin filament elongation regulate the WAVE complex during cell migration. Nat Cell Biol *23*, 1148-1162. 10.1038/s41556-021-00786-8.
71. Orré, T., Joly, A., Karatas, Z., Kastberger, B., Cabriel, C., Böttcher, R.T., Lévêque-Fort, S., Sibarita, J.B., Fässler, R., Wehrle-Haller, B., et al. (2021). Molecular motion and tridimensional nanoscale localization of kindlin control integrin activation in focal adhesions. Nature communications *12*, 3104. 10.1038/s41467-021-23372-w.
72. Pol, A., Morales-Paytuví, F., Bosch, M., and Parton, R.G. (2020). Non-caveolar caveolins - duties outside the caves. J Cell Sci *133*. 10.1242/jcs.241562.
73. Orre, T., Mehidi, A., Massou, S., Rossier, O., and Giannone, G. (2018). Using Single-Protein Tracking to Study Cell Migration. Methods in molecular biology (Clifton, N.J.) *1749*, 291-311. 10.1007/978-1-4939-7701-7_21.
74. Ouyang, W., Aristov, A., Lelek, M., Hao, X., and Zimmer, C. (2018). Deep learning massively accelerates super-resolution localization microscopy. Nature biotechnology *36*, 460-468. 10.1038/nbt.4106.
75. Schermelleh, L., Ferrand, A., Huser, T., Eggeling, C., Sauer, M., Biehlmaier, O., and Drummen, G.P.C. (2019). Super-resolution microscopy demystified. Nat Cell Biol *21*, 72-84. 10.1038/s41556-018-0251-8.
76. Khater, I.M., Nabi, I.R., and Hamarneh, G. (2020). A Review of Super-Resolution Single-Molecule Localization Microscopy Cluster Analysis and Quantification Methods. Patterns (N Y) *1*, 100038. 10.1016/j.patter.2020.100038.
77. Möckl, L., Roy, A.R., and Moerner, W.E. (2020). Deep learning in single-molecule microscopy: fundamentals, caveats, and recent developments [Invited]. Biomedical optics express *11*, 1633-1661. 10.1364/boe.386361.
78. Nunes Vicente, F., Chen, T., Rossier, O., and Giannone, G. (2023). Novel imaging methods and force probes for molecular mechanobiology of cytoskeleton and adhesion. Trends Cell Biol *33*, 204-220. 10.1016/j.tcb.2022.07.008.
79. Monier, S., Parton, R.G., Vogel, F., Behlke, J., Henske, A., and Kurzchalia, T.V. (1995). VIP21-caveolin, a membrane protein constituent of the caveolar coat, oligomerizes in vivo and in vitro. Mol Biol Cell *6*, 911-927.
80. Pelkmans, L., and Zerial, M. (2005). Kinase-regulated quantal assemblies and kiss-and-run recycling of caveolae. Nature *436*, 128-133.
81. Massou, S., Nunes Vicente, F., Wetzel, F., Mehidi, A., Strehle, D., Leduc, C., Voituriez, R., Rossier, O., Nassoy, P., and Giannone, G. (2020). Cell stretching is amplified by active

actin remodelling to deform and recruit proteins in mechanosensitive structures. Nature Cell Biology. 10.1038/s41556-020-0548-2.

82. Shivanandan, A., Radenovic, A., and Sbalzarini, I.F. (2013). MosaicIA: an ImageJ/Fiji plugin for spatial pattern and interaction analysis. BMC Bioinformatics *14*, 349. 10.1186/1471-2105-14-349.
83. Sens, P., and Turner, M.S. (2004). Theoretical model for the formation of caveolae and similar membrane invaginations. Biophys J *86*, 2049-2057. 10.1016/s0006-3495(04)74266-6.
84. Dulhunty, A.F., and Franzini-Armstrong, C. (1975). The relative contributions of the folds and caveolae to the surface membrane of frog skeletal muscle fibres at different sarcomere lengths. J Physiol *250*, 513-539.
85. Prescott, L., and Brightman, M.W. (1976). The sarcolemma of Aplysia smooth muscle in freeze-fracture preparations. Tissue Cell *8*, 248-258.
86. Gabella, G., and Blundell, D. (1978). Effect of stretch and contraction on caveolae of smooth muscle cells. Cell and tissue research *190*, 255-271.
87. Qifti, A., Balaji, S., and Scarlata, S. (2022). Deformation of caveolae impacts global transcription and translation processes through relocalization of cavin-1. J Biol Chem *298*, 102005. 10.1016/j.jbc.2022.102005.
88. McMahon, K.A., Stroud, D.A., Gambin, Y., Tillu, V., Bastiani, M., Sierecki, E., Polinkovsky, M.E., Hall, T.E., Gomez, G.A., Wu, Y., et al. (2021). Cavin3 released from caveolae interacts with BRCA1 to regulate the cellular stress response. eLife *10*, e61407. 10.7554/eLife.61407.
89. Okada, S., Raja, S.A., Okerblom, J., Boddu, A., Horikawa, Y., Ray, S., Okada, H., Kawamura, I., Murofushi, Y., Murray, F., and Patel, H.H. (2019). Deletion of caveolin scaffolding domain alters cancer cell migration. Cell Cycle *18*, 1268-1280. 10.1080/15384101.2019.1618118.
90. Jasmin, J.F., Mercier, I., Sotgia, F., and Lisanti, M.P. (2006). SOCS proteins and caveolin-1 as negative regulators of endocrine signaling. Trends in endocrinology and metabolism: TEM *17*, 150-158. 10.1016/j.tem.2006.03.007.
91. Kershaw, N.J., Murphy, J.M., Lucet, I.S., Nicola, N.A., and Babon, J.J. (2013). Regulation of Janus kinases by SOCS proteins. Biochem Soc Trans *41*, 1042-1047. 10.1042/bst20130077.
92. Williams, J.J.L., Alotaiq, N., Mullen, W., Burchmore, R., Liu, L., Baillie, G.S., Schaper, F., Pilch, P.F., and Palmer, T.M. (2018). Interaction of suppressor of cytokine signalling 3 with cavin-1 links SOCS3 function and cavin-1 stability. Nature communications *9*, 168. 10.1038/s41467-017-02585-y.
93. Byrne, D.P., Dart, C., and Rigden, D.J. (2012). Evaluating caveolin interactions: do proteins interact with the caveolin scaffolding domain through a widespread aromatic residue-rich motif? PLoS One *7*, e44879. 10.1371/journal.pone.0044879.
94. Collins, B.M., Davis, M.J., Hancock, J.F., and Parton, R.G. (2012). Structure-based reassessment of the caveolin signaling model: do caveolae regulate signaling through caveolin-protein interactions? Dev Cell *23*, 11-20.
95. Jung, W., Sierecki, E., Bastiani, M., O'Carroll, A., Alexandrov, K., Rae, J., Johnston, W., Hunter, D.J.B., Ferguson, C., Gambin, Y., et al. (2018). Cell-free formation and interactome analysis of caveolae. J Cell Biol *217*, 2141-2165. 10.1083/jcb.201707004.
96. Kenworthy, A.K., Han, B., Ariotti, N., and Parton, R.G. (2023). The Role of Membrane Lipids in the Formation and Function of Caveolae. Cold Spring Harbor perspectives in biology. 10.1101/cshperspect.a041413.
97. Han, B., Porta, J.C., Hanks, J.L., Peskova, Y., Binshtein, E., Dryden, K., Claxton, D.P., McHaourab, H.S., Karakas, E., Ohi, M.D., and Kenworthy, A.K. (2020). Structure and

assembly of CAV1 8S complexes revealed by single particle electron microscopy. Sci Adv *6*. 10.1126/sciadv.abc6185.

98. Lim, J.E., Bernatchez, P., and Nabi, I.R. (2024). Scaffolds and the scaffolding domain: an alternative paradigm for caveolin-1 signaling. Biochem Soc Trans *52*, 947-959. 10.1042/bst20231570.
99. Doktorova, M., Daum, S., Ebenhan, J., Neudorf, S., Han, B., Sharma, S., Kasson, P., Levental, K., Bacia, K., Kenworthy, A.K., and Levental, I. (2024). Caveolin assemblies displace one bilayer leaflet to organize membranes. BioRxv.
100. Wong, T.H., Khater, I.M., Joshi, B., Shahsavari, M., Hamarneh, G., and Nabi, I.R. (2021). Single molecule network analysis identifies structural changes to caveolae and scaffolds due to mutation of the caveolin-1 scaffolding domain. Scientific reports *11*. 10.1038/s41598-021-86770-6.
101. Shan, M., Zhao, X., Sun, P., Qu, X., Cheng, G., and Qin, L.P. (2024). Revisiting Structure-activity Relationships: Unleashing the potential of selective Janus kinase 1 inhibitors. Bioorg Chem *149*, 107506. 10.1016/j.bioorg.2024.107506.
102. Dewulf, M., Koster, D.V., Sinha, B., Viaris de Lesegno, C., Chambon, V., Bigot, A., Bensalah, M., Negroni, E., Tardif, N., Podkalicka, J., et al. (2019). Dystrophy-associated caveolin-3 mutations reveal that caveolae couple IL6/STAT3 signaling with mechanosensing in human muscle cells. Nature communications *10*, 1974. 10.1038/s41467-019-09405-5.
103. Owen, K.L., Brockwell, N.K., and Parker, B.S. (2019). JAK-STAT Signaling: A Double-Edged Sword of Immune Regulation and Cancer Progression. Cancers *11*. 10.3390/cancers11122002.
104. Friedland, J.C., Lee, M.H., and Boettiger, D. (2009). Mechanically activated integrin switch controls alpha5beta1 function. Science *323*, 642-644. 10.1126/science.1168441.
105. Giannone, G., Jiang, G., Sutton, D.H., Critchley, D.R., and Sheetz, M.P. (2003). Talin1 is critical for force-dependent reinforcement of initial integrin-cytoskeleton bonds but not tyrosine kinase activation. J Cell Biol *163*, 409-419. 10.1083/jcb.200302001.
106. Jiang, G., Giannone, G., Critchley, D.R., Fukumoto, E., and Sheetz, M.P. (2003). Two-piconewton slip bond between fibronectin and the cytoskeleton depends on talin. Nature *424*, 334-337. 10.1038/nature01805.
107. Wang, Y., Botvinick, E.L., Zhao, Y., Berns, M.W., Usami, S., Tsien, R.Y., and Chien, S. (2005). Visualizing the mechanical activation of Src. Nature *434*, 1040-1045. 10.1038/nature03469.
108. del Rio, A., Perez-Jimenez, R., Liu, R., Roca-Cusachs, P., Fernandez, J.M., and Sheetz, M.P. (2009). Stretching single talin rod molecules activates vinculin binding. Science *323*, 638-641. 10.1126/science.1162912.
109. Sawada, Y., Tamada, M., Dubin-Thaler, B.J., Cherniavskaya, O., Sakai, R., Tanaka, S., and Sheetz, M.P. (2006). Force sensing by mechanical extension of the Src family kinase substrate p130Cas. Cell *127*, 1015-1026. 10.1016/j.cell.2006.09.044.
110. Gordon, W.R., Zimmerman, B., He, L., Miles, L.J., Huang, J., Tiyanont, K., McArthur, D.G., Aster, J.C., Perrimon, N., Loparo, J.J., and Blacklow, S.C. (2015). Mechanical Allostery: Evidence for a Force Requirement in the Proteolytic Activation of Notch. Dev Cell *33*, 729-736. 10.1016/j.devcel.2015.05.004.
111. Iskratsch, T., Wolfenson, H., and Sheetz, M.P. (2014). Appreciating force and shape-the rise of mechanotransduction in cell biology. Nat Rev Mol Cell Biol *15*, 825-833. 10.1038/nrm3903.
112. Ladoux, B., and Mège, R.M. (2017). Mechanobiology of collective cell behaviours. Nat Rev Mol Cell Biol *18*, 743-757. 10.1038/nrm.2017.98.
113. Kirby, T.J., and Lammerding, J. (2018). Emerging views of the nucleus as a cellular mechanosensor. Nat Cell Biol *20*, 373-381. 10.1038/s41556-018-0038-y.

114. del Pozo, M.A., Balasubramanian, N., Alderson, N.B., Kiosses, W.B., Grande-García, A., Anderson, R.G., and Schwartz, M.A. (2005). Phospho-caveolin-1 mediates integrin-regulated membrane domain internalization. Nat Cell Biol *7*, 901-908. 10.1038/ncb1293.
115. Osmani, N., Pontabry, J., Comelles, J., Fekonja, N., Goetz, J.G., Riveline, D., Georges-Labouesse, E., and Labouesse, M. (2018). An Arf6- and caveolae-dependent pathway links hemidesmosome remodeling and mechanoresponse. Mol Biol Cell *29*, 435-451. 10.1091/mbc.E17-06-0356.
116. Muriel, O., Echarri, A., Hellriegel, C., Pavon, D.M., Beccari, L., and Del Pozo, M.A. (2011). Phosphorylated filamin A regulates actin-linked caveolae dynamics. J Cell Sci *124*, 2763-2776.
117. Goetz, J.G., Joshi, B., Lajoie, P., Strugnell, S.S., Scudamore, T., Kojic, L.D., and Nabi, I.R. (2008). Concerted regulation of focal adhesion dynamics by galectin-3 and tyrosine-phosphorylated caveolin-1. J Cell Biol *180*, 1261-1275.
118. Gottlieb-Abraham, E., Shvartsman, D.E., Donaldson, J.C., Ehrlich, M., Gutman, O., Martin, G.S., and Henis, Y.I. (2013). Src-mediated caveolin-1 phosphorylation affects the targeting of active Src to specific membrane sites. Mol Biol Cell *24*, 3881-3895. 10.1091/mbc.E13-03-0163.
119. Zimnicka, A.M., Husain, Y.S., Shajahan, A.N., Sverdlov, M., Chaga, O., Chen, Z., Toth, P.T., Klomp, J., Karginov, A.V., Tiruppathi, C., et al. (2016). Src-dependent phosphorylation of caveolin-1 Tyr-14 promotes swelling and release of caveolae. Mol Biol Cell *27*, 2090-2106. 10.1091/mbc.E15-11-0756.
120. Joshi, B., Bastiani, M., Strugnell, S.S., Boscher, C., Parton, R.G., and Nabi, I.R. (2012). Phosphocaveolin-1 is a mechanotransducer that induces caveola biogenesis via Egr1 transcriptional regulation. J Cell Biol *199*, 425-435. 10.1083/jcb.201207089.
121. Sotodosos-Alonso, L., Pulgarín-Alfaro, M., and Del Pozo, M.A. (2023). Caveolae Mechanotransduction at the Interface between Cytoskeleton and Extracellular Matrix. Cells *12*. 10.3390/cells12060942.
122. Goetz, J.G., Lajoie, P., Wiseman, S.M., and Nabi, I.R. (2008). Caveolin-1 in tumor progression: the good, the bad and the ugly. Cancer metastasis reviews *27*, 715-735.
123. Lamaze, C., and Torrino, S. (2015). Caveolae and Cancer: A New Mechanical Perspective. Biomedical journal *38*, 367-379. 10.4103/2319-4170.164229.
124. Simón, L., Campos, A., Leyton, L., and Quest, A.F.G. (2020). Caveolin-1 function at the plasma membrane and in intracellular compartments in cancer. Cancer metastasis reviews *39*, 435-453. 10.1007/s10555-020-09890-x.
125. Heilemann, M., van de Linde, S., Schüttpelz, M., Kasper, R., Seefeldt, B., Mukherjee, A., Tinnefeld, P., and Sauer, M. (2008). Subdiffraction-resolution fluorescence imaging with conventional fluorescent probes. Angewandte Chemie (International ed. in English) *47*, 6172-6176. 10.1002/anie.200802376.
126. Lampe, A., Tadeus, G., and Schmoranzer, J. (2015). Spectral demixing avoids registration errors and reduces noise in multicolor localization-based super-resolution microscopy. Methods Appl Fluoresc *3*, 034006. 10.1088/2050-6120/3/3/034006.
127. Nunes Vicente, F., Lelek, M., Tinevez, J.Y., Tran, Q.D., Pehau-Arnaudet, G., Zimmer, C., Etienne-Manneville, S., Giannone, G., and Leduc, C. (2022). Molecular organization and mechanics of single vimentin filaments revealed by super-resolution imaging. Sci Adv *8*, eabm2696. 10.1126/sciadv.abm2696.
128. Schnitzbauer, J., Strauss, M.T., Schlichthaerle, T., Schueder, F., and Jungmann, R. (2017). Super-resolution microscopy with DNA-PAINT. Nature protocols *12*, 1198-1228. 10.1038/nprot.2017.024.
129. Levet, F., Hosy, E., Kechkar, A., Butler, C., Beghin, A., Choquet, D., and Sibarita, J.B. (2015). SR-Tesseler: a method to segment and quantify localization-based super-resolution microscopy data. Nat Methods *12*, 1065-1071. 10.1038/nmeth.3579.

130. Izeddin, I., Boulanger, J., Racine, V., Specht, C.G., Kechkar, A., Nair, D., Triller, A., Choquet, D., Dahan, M., and Sibarita, J.B. (2012). Wavelet analysis for single molecule localization microscopy. Opt Express *20*, 2081-2095. 10.1364/oe.20.002081.
131. Racine, V., Sachse, M., Salamero, J., Fraisier, V., Trubuil, A., and Sibarita, J.B. (2007). Visualization and quantification of vesicle trafficking on a three-dimensional cytoskeleton network in living cells. Journal of microscopy *225*, 214-228. 10.1111/j.1365-2818.2007.01723.x.
132. Racine, V., Hertzog, A., Jouanneau, J., Salamero, J., Kervrann, C., and Sibarita, J.B. (2006). Multiple-target tracking of 3D fluorescent objects based on simulated annealing. 6-9 April 2006. pp. 1020-1023.
133. Cheezum, M.K., Walker, W.F., and Guilford, W.H. (2001). Quantitative comparison of algorithms for tracking single fluorescent particles. Biophys J *81*, 2378-2388. 10.1016/s0006-3495(01)75884-5.
134. Waterhouse, A., Bertoni, M., Bienert, S., Studer, G., Tauriello, G., Gumienny, R., Heer, F.T., de Beer, T.A.P., Rempfer, C., Bordoli, L., et al. (2018). SWISS-MODEL: homology modelling of protein structures and complexes. Nucleic Acids Res *46*, W296-w303. 10.1093/nar/gky427.
135. Caveney, N.A., Saxton, R.A., Waghray, D., Glassman, C.R., Tsutsumi, N., Hubbard, S.R., and Garcia, K.C. (2023). Structural basis of Janus kinase trans-activation. Cell reports *42*, 112201. 10.1016/j.celrep.2023.112201.
136. Honorato, R.V., Koukos, P.I., Jiménez-García, B., Tsaregorodtsev, A., Verlato, M., Giachetti, A., Rosato, A., and Bonvin, A. (2021). Structural Biology in the Clouds: The WeNMR-EOSC Ecosystem. Front Mol Biosci *8*, 729513. 10.3389/fmolb.2021.729513.
137. van Zundert, G.C.P., Rodrigues, J., Trellet, M., Schmitz, C., Kastritis, P.L., Karaca, E., Melquiond, A.S.J., van Dijk, M., de Vries, S.J., and Bonvin, A. (2016). The HADDOCK2.2 Web Server: User-Friendly Integrative Modeling of Biomolecular Complexes. Journal of molecular biology *428*, 720-725. 10.1016/j.jmb.2015.09.014.

Methods

Cell culture, transfection and cell treatments

All cell lines were cultured at 37°C under 5% CO_2 in their respective culture media. Wild-type (WT) and *CAV1*$^{-/-}$ mouse lung endothelial cell lines (MLECs) [a gift from Radu.V. Stan] were cultured in Endothelial Cell Growth Medium-2 (EGM™-2) Bulletkit™ (Lonza, cat. #CC-3162) composed of EBM-2 Basal Medium (cat. #CC-3156) and supplemented with EGM-2 SingleQuots™ (cat. #CC-4176) containing hydrocortisone, hFGF-B, VEGF, R3-IGF-1, ascorbic acid, hEGF, GA-1000 (Gentamicin, Amphotericin-B) and heparin along with 10% FBS (Gibco, Life Technologies). All Murine Embryonic Fibroblast cell lines used in this study (MEF WT, MEF Cavin1$^{-/-}$ and MEF Cavin1$^{-/-}$ expressing low/medium/high levels of Cav1) [a gift from Miguel del Pozo] were cultured in Dulbecco's modified Eagle medium (DMEM) GlutaMAX™ (Gibco, Life Technologies) supplemented with 10% FBS (Gibco, Life Technologies), 100 U/ml penicillin-streptomycin, 1 mM sodium pyruvate and 15 mM HEPES.

Plasmids were transfected either by electroporation using Ingenio® electroporation solution (Mirus Bio LLC) or by lipofection using Lipofectamine LTX with Plus reagent (Invitrogen, Life Technologies), Lipofectamine 3000 (Invitrogen, Life Technologies) or HiPerFect transfection reagents (Qiagen Inc.) following the manufacturer's instructions. Electroporation of cells was performed with a pulse of 220 V and 975 µF using a Gene Pulser II module (Bio-Rad). siRNA transfections were performed using the HiPerFect kit and cells were incubated for 3 days before further experimentation. Depletion efficiency was assessed by immunoblotting.

Unless otherwise stated, stimulation with IFN-α or IFN-β (recombinant mouse IFN-α;

BioLegend cat. #752806, mouse IFN-β; tebubio cat. #12400-1) was performed at a concentration of 1000 U/ml and 500 U/ml respectively. For cell stretching experiments, cells were grown on a rectangular PDMS sheet (thickness ~100 µm, dimensions ~12 × 7 mm) coated with fibronectin and stretched uni-axially using a custom-built device equipped with a motorized linear actuator (PI, Karlsruhe, Germany) and a temperature controller. Cells were pre-stretched by 25% for 2 minutes and stretch was maintained during IFN-α stimulation. For hypo-osmotic shock (HYPO), cells were subjected to culture media diluted in water and processed for subsequent experiments. Unless otherwise stated, cells were subjected to 30 mOsm hypo-osmotic shock (10% culture media and 90% water) for a duration of 5 minutes. Recovery (REC) of cells were performed by first subjecting the cells to a 5-min hypo-osmotic shock and immediately replenishing with normal culture media (300 mOsm). Unless otherwise stated, recovery (REC) is performed for a duration of 5 minutes post hypo-osmotic shock.

Plasmids and antibodies

Cav1-GFP and cavin-1-mEGFP were a gift from Ari Helenius (Addgene plasmid # 14433; https://n2t.net/addgene:14433; RRID: Addgene_14433 and Addgene plasmid # 27709; http://n2t.net/addgene:27709; RRID: Addgene_27709 respectively). Cav1-RFP and Cav1F92A/V94A-RFP plasmids are described elsewhere [37]. mEos3.2-Caveolin-C-10 was a gift from Michael Davidson (Addgene plasmid # 57447; http://n2t.net/addgene:57447; RRID: Addgene 57447). mEos2-CAAX was generated by amplifying the coding DNA sequence of the corresponding protein by PCR and inserted into the pcDNAm-FRT-PC-mEos2 blue at Fse1/Asc1 sites. For the generation of ALFA-tagged JAK1WT, JAK1-stopCBM3 and JAK1-stop-ΔCBM3 constructs, JAK1 was first amplified with primers

containing the ALFA-tag sequence. The amplicon was then cloned into a pmCherry-C vector backbone devoid of the mCherry sequence. Subsequently, point-mutations were introduced at the desired residues by site-directed mutagenesis to generate the respective mutants. The fidelity of all constructs was verified by sequencing.

The following primary antibodies were used: mouse anti-a-tubulin (Sigma-Aldrich, clone B512, Cat. #T5168, 1:1000 for WB); mouse anti-CHC (BD Transduction, Cat. #610500, 1:5000 for WB); mouse anti-STAT3 (Cell signaling, clone 124H6, Cat. #9139, 1:1000 for WB); rabbit anti-pSTAT3 (Tyr705) (Cell signaling technologies, clone D3A7, Cat. #9145, 1:1000 for WB, 1:100 for IF); rabbit anti-STAT1 (Cell signaling technologies, Cat. #9172, 1:1000 for WB); mouse anti-pSTAT1 (Tyr701) (Cell signaling technologies, clone 58D6, Cat. #9167, 1:1000 for WB, 1:100 for IF); mouse anti-Cav1 (BD Transduction, Cat. #610407, 1:1000 for WB); rabbit anti-Cav1 (Cell Signaling Technologies Cat. #3238S, 1:1000 for WB, 2-5 µg/condition for IP, 1:50 for dSTORM, 1:150 for IF); mouse anti-PTRF (BD Transduction Cat. #611258, 1:1000 for WB); rabbit anti-PTRF (Cat. #ab48824, Abcam – discontinued, 1:1000 for WB, 1:50 for dSTORM, 1:150 for IF); rabbit anti-JAK1 (Cell signaling technologies, Cat. #3332S, 1:2000 for WB); mouse anti-JAK1 (Santa Cruz Biotechnology, Cat. #sc-1677, 1:50 for STORM); rabbit anti-eNOS (Cell signaling technologies Cat. #32027S, 1:2000 for WB); rabbit anti-PTEN (Cell signaling technologies Cat. #9188S, 1:2000 for WB); rabbit anti-AKT (Cell signaling technologies Cat. #9272S, 1:2000 for WB); rabbit anti-pAKT (Ser473) (Cell signaling technologies Cat. #4060S, 1:2000 for WB); rabbit anti-PTP1B (Abcam Cat. #ab244207, 1:2000 for WB); rabbit anti-β1-integrin (Proteintech Cat. #12594-1-AP); rabbit anti-mCherry (Institut Curie Recombinant antibody platform, A-P-R #13).

The following secondary antibodies were used: Donkey anti-mouse-HRP (Jackson ImmunoResearch, cat. #715-035-151) and Donkey anti-rabbit-HRP (Jackson ImmunoResearch, cat. #711-035-152) were used at a dilution of 1:5,000 for WB; Donkey anti-mouse-AF647 (Jackson ImmunoResearch, cat. #715-606-150) and Donkey anti-rabbit-CF680 (Biotium, cat. #20820) were used at a dilution of 1:200 and 1:400 respectively, for STORM imaging.

RNA interference-mediated silencing

Except when stated otherwise, siRNAs were used at a concentration of 20 nM. Depletion efficiency was assessed by immunoblotting. SMART pool siRNA targeting *Mus musculus* JAK1 mRNA (Dharmacon, Cat. No: L-040117-00-0005) was used for JAK1 knock down. Scramble siRNA (QIAGEN, Cat. No: 1022076) was used as a control.

High Throughput screening

25 µg/mL fibronectin diluted in NaOH 100 mM pH 8.6 is incubated on a PDMS layer at 37°C. 70k WT MLEC or MLEC *Cav1*$^{-/-}$ cells were seeded and incubated for 4 hours at 37°C in complete MLEC media. Cells were stretched by 25% for 2 minutes then while stretch is maintained, cells media is replaced by stimulation media (EBM-2 no SVF with IFN-α 1000 U/ml) for 20 min at 37°C. Cells were washed with PBS and lysed with hot Laemmli 1X sample buffer (50 mM Tris pH=6.8, 2% SDS, 5% glycerol, 2 mM DTT, 2,5 mM EDTA, 2.5 mM/EGTA, 2.5mM/EGTA, 2x Phosphatase inhibitors (Halt Phosphatase inhibitor cocktail 100x, Perbio, Ref. 78420), Protease inhibitors (Protease inhibitor cocktail, complete MINI EDTA-free, Roche, Ref. 1836170), 1 tablet/5 mL, 4 mM Sodium Orthovanadate, 20 mM Sodium Fluoride) and subjected to Reverse Phase Protein Array analysis.

CSD mimicking peptides

CSD mimicking peptides were synthetized from Biomatik. Control peptide sequence: HHHHHH-RQIKIWFQNRRMKWKKWGIDKASFTTFTVTKYWFRY; CavTratin sequence: HHHHHH-QIKIWFQNRRMKWKKDGIWKASFTTFTVTKY; CavNoxin sequence: HHHHH H-RQIKIWFQNRRMKWKKDGIWKASFAAATVTKWYFYR. Cells were treated for 6 hours with 1 µM CSD mimicking peptide resuspended in EGM-2 culture medium.

In vitro Kinase activity measurement

In-vitro kinase assay was performed using purified JAK1 (ProQinase 1480-0000-1 JAK1 aa583-1154), RBER-IRStide (ProQinase 0863-0000-1). Kinase reaction was performed in Kinase reaction buffer ([ATP] 100 µM, RBER-IRStide 80 µg/ml, DMSO according to peptide concentration) at 30°C for 1 hr. Measurement of ADP production was performed using Promega ADP-Glo™ Kinase Assay. Luminescence measurement was performed using BMG Labtech FLUOstar Omega plate reader.

Immunoblotting

Cells were lysed in sample buffer (62.5 mM Tris–HCl, pH 6.0, 2% (vol/vol) SDS, 10% (vol/vol) glycerol, 40 mM dithiothreitol and 0.03% (wt/vol) phenol red). The lysates were analysed by SDS–PAGE on 4–20% mini-PROTEAN TGX or TGX stain-free precast protein gels (Bio-Rad), and immunoblotted with the indicated primary and secondary antibodies that were either horseradish peroxidase-conjugated or fluorescently labelled. The chemiluminescence signal was revealed using Pierce ECL western blotting, SuperSignal west dura extended duration or SuperSignal west femto (Thermo Scientific Life Technologies) substrate. Acquisition and quantification were performed using a ChemiDoc MP imaging system (Bio-Rad). For STAT1, the phosphorylated and total

protein levels were assayed on the same blot with the primary antibodies mouse anti-pSTAT1 and rabbit anti-STAT1, and visualized using fluorescence and luminescence, respectively. The ratio of phosphorylated-to-total protein was determined for each time point.

Immunofluorescence

For immunofluorescence analysis, cells were either cultured on coverslips or PDMS as per the experimental procedure, treated as described earlier and then fixed with ice-cold methanol for 15 min at -20°C. After washing with 0.2% (wt/vol) BSA in PBS, the cells were subsequently incubated with the indicated primary antibody and fluorescence-conjugated secondary antibody for 1h at room temperature. The coverslips were mounted in Fluoromount-G mounting medium (eBioscience) with 2 µg/ml 4,6-diamidino-2-phenylindole (Sigma-Aldrich) to counterstain nuclei. Images were acquired on a Leica DM 6000B inverted wide-field microscope equipped with a HCX PL Apo ×63, 1.40 numerical aperture (NA) oil immersion objective and an electron-multiplying charge-coupled device (CCD) camera (Photometrics CoolSMAP HQ). Nuclear translocation of pSTAT1/pSTAT3 was quantified using a homemade plugin in the ImageJ software (NIH) by calculating the nuclear-to-cytoplasmic ratio of the pSTAT1 signal (nuclei masks were realized with 4,6-diamidino-2-phenylindole staining).

Co-immunoprecipitation

Cells were lysed in 1% NP-40 in ice-cold TNE (10 mM Tris–HCl pH 7.5, 150 mM NaCl and 0.5 mM EDTA) with protease inhibitor cocktail (Roche) for 30 min. For conventional co-immunoprecipitation, cleared lysates (16,000g for 10 min at 4 °C) were incubated overnight with 1 µg/ml of the indicated antibody at 4 °C, with rotation, followed by

incubation for 1 h with 25 µl protein A/G magnetic beads (Thermo Scientific) in the case of endogenous proteins. For tagged proteins, 25 µl of GFP-Trap or RFP-Trap beads (Chromotek) were used. After three washes in TNE, the immunoprecipitated beads were eluted following the manufacturer's instructions. Magnetic crosslink co-immunoprecipitation (Pierce™ Crosslink Magnetic IP/Co-IP Kit, cat. #88805) was performed as per the manunfacturer's instruction. Briefly, the desired antibody was covalently crosslinked to protein A/G magnetic beads using the DSS (disuccinimidyl suberate) crosslinker and subsequently incubated overnight with pre-cleared lysates at 4 °C. Incubated beads were then eluted and the immunoprecipitates were anlayzed by immunoblotting.

dSTORM sample preparation

MLEC WT cells grown on high resolution #1.5 glass coverslips (THOR labs) were washed three times with PHEM solution (60 mM PIPES, 25 mM HEPES, 5 mM EGTA and 2 mM Mg acetate adjusted to pH 6.9 with 1 M KOH) and fixed for 20 min in 4% PFA. They were then washed 3 times in PBS (137 mM NaCl, 2.7 mM KCl, 8 mM Na_2HPO_4, and 2 mM KH_2PO_4). Up to this fixation step, all chemical reagents were pre- warmed at 37°C. The cells were then quenched for auto-fluorescence from PFA in 50 mM NH_4Cl for 20 min at RT. The cells were washed in PBS three times before being blocked and permeabilized in blocking buffer (1X PBS / 1% BSA / 0.1% Saponin) for 1 hr at RT. Fixed cells were incubated for 1 hr at 37°C with the respective primary antibodies diluted in blocking buffer and washed three times with PBS. This was followed by 1 hr incubation at 37°C with corresponding secondary antibodies diluted in blocking buffer and washed three times with PBS. After immunolabelling, a post-fixation step was performed using PBS with 3.6%

formaldehyde for 15 min. The cells were washed in PBS three times and then reduced for 10 min with 50 mM NH_4Cl (Sigma Aldrich, 254134), followed by three additional washes in PBS.

Dual color dSTORM imaging

Fluorophores Alexa-Fluor™ 647 (AF647) and CF680 photo switch under reducing and oxygen-free buffer conditions, making them suitable for dSTORM single molecule imaging, which enables the localization of the emitters with sub-diffraction localization precision [125]. Thanks to their close spectral proximity, AF647 was excited and acquired simultaneously with CF680 in the same dSTORM buffer (Abbelight™ SMART-Kit) using a 640 nm laser (Oxxius), and their respective signals discriminated after single molecule localization using a spectral demixing strategy [126]. To implement spectral demixing dSTORM of JAK1-A647 and Cav1-CF680, we used a dual-view Abbelight™ SAFe360, equipped with two Hamamatsu Fusion sCMOS cameras and mounted on an Olympus Ix83 inverted microscope with a 100X 1.5NA TIRF objective. The SAFe360 uses astigmatic PSF engineering to extract the axial position and achieves quasi-isotropic 3D localization precision, and a long-pass dichroic mirror to split fluorescence from single emitters on the two cameras. Samples were illuminated in HILO at 80% of max laser power and imaged at 50 ms exposure time for 100000 frames. Single molecule localization, drift correction, spectral demixing and data visualization were performed using Abbelight™ NEO software.

3D SMLM network analysis

A total of 30 cells (15 cells each for ISO and HYPO conditions) stained for Cav1-CF680 and JAK1-AF647 were imaged using the Abbelight SAFe 360 microscope utilizing the

spectral demixing technique. Cav1 localizations were processed, and the resulting clusters were classified using the 3D SMLM network analysis pipeline described in [39]. The datasets were analyzed using the 3D SMLM network analysis based on the following parameters: merging threshold = 19 nm (to correct multiple blinking of single fluorophores); proximity threshold = 80 nm (for network construction); alpha = 2 (for noise filtering); bandwidth = 120 nm (for segmenting the localization into blobs/clusters using mean shift algorithm). Following this, 28 features/descriptors (shape, topology, network, size, hollowness, etc.) were extracted for every segmented blob/cluster. The clusters/blobs feature of every condition were then grouped into four groups using the x-means algorithm. The biological names for the groups i.e., caveolae and S2, S1A, and S1B scaffolds, were obtained by comparing the group centers with the Cav1 groups that were obtained previously in [39] and were assigned based on the best match (highest similarity).

Spatial pattern and interaction analysis

The interaction analysis was performed using the MosaicIA plugin [82] for Fiji by loading the 3D co-ordinates of JAK1 and the center of mass of the corresponding Cav1 clusters identified using the 3D SMLM network analysis pipeline (namely caveolae, S2, S1B and S1A scaffolds) from a total of 30 cells (15 cells each for ISO and HYPO condition) and selecting 2 random ROIs from each cell. The workflow for interaction analysis described in [82] was followed. The following parameters were used for computing distance distributions: Grid spacing = 0.2 (this value was chosen by sequentially reducing the grid spacing until the q(d) does not significantly change); Kernel wt(q) = 0.001; Kernel wt(p) was used as suggested by the software. To determine the best parametric potential for

the dataset, a non-parametric potential was first used to estimate the shape of interaction. The various available parametric potentials were then tested to determine the one that best fits the estimated shape of interaction. The Linear L1 potential resulted in the best fit and hence was used for subsequent datasets. The strength of interaction was plotted for each Cav1 cluster type under ISO and HYPO conditions.

Co-localization/nearest localization using distance to centroid

The open-source software Point Cloud Analyst (PoCA) [https://github.com/flevet/ PoCA] was used to determine the distance to centroids between objects of interest (i.e. between JAK1 and the various classes of Cav1 clusters) within a defined ROI. In brief, the 3D coordinates of JAK1 and Cav1 clusters (namely caveolae, S2, S1B and S1A scaffolds) identified using the 3D SMLM network analysis pipeline were loaded individually and the corresponding voronoi diagram or tessellation was generated using an in-built algorithm. For creating objects from the voronoi tessellations, a cut-off threshold of 75 and 100 with a minimum number of localizations of 2 and 11 was used for JAK1 and Cav1 respectively. The centroids of the resulting objects were extracted following which the centroids of JAK1 and the various Cav1 cluster objects were superimposed in pairs (eg: JAK1-Caveolae, JAK1-S2, JAK1-S1B and JAK1-S1A). The distance to centroids for each pair was calculated within several defined ROIs using the Cav1 cluster centroids as the reference i.e. the distance computation was done between JAK1 objects (centroids) and the outline of the reference (Cav1 objects).

Micromechanical stretching device compatible with super-resolution microscopy

The stretching device compatible with super-resolution microscopy (used for DNA-PAINT and single particle tracking in the current manuscript) has been described previously

[81,127]. Briefly, a plasma-cleaned polydimethylsiloxane (PDMS) sheet (10 µm; Sylgard 184, DE9330, Samaro) was deposited on a plasma-cleaned glass coverslip, lubricated by a thin layer of low-viscous glycerol (glycerol for fluorescence microscopy; CAS 56-81-5; Merck; 1040950250), and reinforced by a thicker elastomer frame (40 µm, PF film X0; 1.5 mil; Gel-Pak). The 40 µm elastomer frame was pre-cut to the size of the glass coverslip with a squared (3 mm × 3 mm) observation chamber using a Graphtec cutting plotter (Graphtec Craft ROBO pro; CE5000-40-CRP). Uniaxial stretch was applied using a milled (Charlyrobot, Mecanumic) poly (methyl methacrylate) (PMMA) device consisting of a fixed holding arm and a mobile arm, positioned on opposite sides of the observation chamber on the elastomer frame. The mobile arm was connected to a mechanical motor (MTS-65, 52mm; Linear stage with stepper motor; 0.1 µm resolution; PI). PDMS substrate was coated with human fibronectin (10 $\mu g.ml^{-1}$) for 90 min at 37°C. Then, after electroporation with Cav1-GFP, MLEC *CAV1*$^{-/-}$ cells were plated on the stretching device and spread overnight at 37°C.

DNA-PAINT acquisition and analysis

The stretching device was mounted on an inverted motorized microscope (Nikon Ti) equipped with a CFI Apochromat TIRF 100× oil, NA 1.49 objective and a perfect focus system (PFS-2). First, live stretching onto the microscope was performed at 37°C. To calibrate the strain on each stretching device, we adsorbed 0.1-µm fluorescent beads (TetraSpeck Microspheres; 0.1 µm; Thermo Fisher Scientific; T7279) on the stretching chamber and used a small stretch (2% to 3%) prior to the stretching protocol. Strain is calculated using distances of same beads before and after stretch: $Strain=(L_{stretch}-L_0)/L_0$, where L_0 is the beads distance before stretch and $L_{stretch}$ is the distance for same beads

after stretch. Then, a uniaxial cyclic stretch (stretch: 30% strain, 0.5 Hz, 30 min) was applied, followed by rapid cell fixation in 4% paraformaldehyde in PBS buffer for 15 min. Then, cells were quenched with glycine (150 mM) for 20 min, and blocked for 90 min with 3% BSA and 0.2% Triton X-100 in PBS, then incubated with GFP nanobody conjugated with a DNA-strand P1 for 4 hours (5' Nanobody GFP - TTA TAC ATC TA 3'), followed by a second fixation with 4% paraformaldehyde and 0.2% glutaraldehyde in PBS for 20 min. DNA-PAINT acquisitions [128] after live stretching and fixation were performed at 25°C in stretching devices on the same microscope. Prior to DNA-PAINT, we acquired low-resolution images of Cav1-GFP. Then, super-resolution imaging was performed thanks to the perfect focus system, allowing long acquisition in TIRF illumination mode, required for single-molecule localization microscopy including DNA-PAINT. To register super-resolution intensity images, we adsorbed 90-nm gold nanoparticles (Cytodiagnostics) on the stretching chamber that were imaged during the entirety of the DNA-PAINT acquisitions. Cy3B-labeled DNA imager strands (5' CTA GAT GTA T - Cy3b 3') were added to the stretching chamber at variable concentrations (0.2 to 1 nM), and visualized with a 561-nm laser (Coherent Obis FP series lasers) with 20 mW power at the sample plane. Fluorescence was collected by the combination of a dichroic filter and emission filters (dichroic, Di01-R561; emission, FF01-617/73; Semrock) and a sensitive scientific complementary metal-oxide semiconductor (ORCA-Flash4.0, Hammamatsu). Cav1-GFP was imaged using a conventional GFP filter cube (excitation, FF01-472/30; dichroic, FF-495Di02; emission, FF02-520/28; Semrock). The acquisitions were steered by MetaMorph software (Molecular Devices) in streaming mode at 100 ms for 90 000 frames. DNA-PAINT image reconstruction and drift correction were carried out using the Picasso

software [128]. The spatial resolution of DNA-PAINT acquisitions obtained on stretching device was ~15.7 ± 1.5 nm (full width at half-maximum (FWHM)). SR-Tesseler [129] was used to segment DNA-PAINT super-resolution images, to obtain the size distribution of Cav1-GFP clusters without stretching, or after cyclic stretching. Single-molecule localizations were used to compute Voronoï diagram. Clusters were segmented using average density factor of 20. To filter background noise of DNA-PAINT acquisitions, often corresponding to unspecific binding of some DNA imager strands to the cover-glass, we set a threshold for the number of localizations (50), enabling to select only genuine signals associated with binding to DNA docking strands. To analyze the smallest Cav1-GFP structures detected using DNA-PAINT, we manually selected isolated clusters that exhibited DNA-PAINT signals throughout the entire acquisition period. The size of these clusters was measured using SR-Tesseler [128].

sptPALM sample preparation

For both MLEC and MEF cells, transient transfections of plasmids were performed 1 day before experiments using the Nucleofactor™ transfection kit for MEF-1 and Nucleofactor™ IIb device (Amaxa™, Lonza). For MLECs, cells were detached with accutase solution (Sigma Aldrich, cat. #SLBT9789). The accutase was inactivated using EGM-2 medium, and the cells were washed and suspended in EGM-2 medium. Cells were then seeded overnight in EGM-2 medium on nitric-acid cleaned glass coverslips. The next day, EGM-2 medium was rinsed once with PBS and left for experiment in serum-free Ringer medium (150 mM NaCl, 5 mM KCl, 2 mM $CaCl_2$, 2 mM $MgCl_2$, 10 mM HEPES, pH=7.4) supplemented with 11 mM glucose. For MEFs, cells were detached with 0.05% trypsin, 0.02% EDTA solution (Gibco Cat. #25300054). The trypsin was inactivated using

soybean trypsin inhibitor (1 mg/ml in DMEM, Sigma), and the cells were washed and suspended in serum-free Ringer medium (150 mM NaCl, 5 mM KCl, 2 mM $CaCl_2$, 2 mM $MgCl_2$, 10 mM HEPES, pH=7.4) supplemented with 11 mM glucose. Cells were then seeded on human fibronectin-coated surface (fibronectin: 10 µg/ml, Roche). MEF PTRF/Cavin1$^{-/-}$ cell line was a gift from Miguel del Pozo (Spanish National Centre for Cardiovascular Research, Spain) and are described elsewhere [41]. Absence of mycoplasma contamination was assessed using the MycoAlert detection kit (Lonza Cat. No. LT07-318). For sptPALM, 120,000 MLEC or 50,000 MEF cells were seeded on #1.5H glass coverslips (Marienfeld). When mentioned, hypo-osmotic shock was induced by replacing the observation medium (Ringer+glucose) with a Ringer+glucose solution diluted 10 times with MQ grade deionized water, at least 5 minutes before acquisition.

sptPALM optical setup and image acquisition

All acquisitions were steered by MetaMorph software (Molecular Devices) with an inverted motorized microscope (Nikon Ti) equipped with a temperature control system (The Cube, The Box, Life Imaging Services), a Nikon CFI Apo TIRF 100x oil, NA 1.49 objective and a perfect focus system, allowing long acquisition in TIRF illumination mode. The coverslip was mounted in a Ludin chamber (Life Imaging Services) before acquisition. For photoactivation localization microscopy, cells expressing mEos3.2 tagged constructs were photoactivated using a 405 nm laser (Omicron) and the resulting photoconverted single molecule fluorescence was excited with a 561 nm laser (Cobolt Jive™). Both lasers illuminated the sample simultaneously. Their respective power was adjusted to keep the number of the stochastically activated molecules constant and well separated during the acquisition. Fluorescence was collected by the combination of a

dichroic and emission filters (D101-R561 and F39-617 respectively; Chroma) and a sensitive EMCCD (electron-multiplying charge-coupled device, Evolve, Photometric). The acquisition was performed in streaming mode at 50 Hz. Cav1-GFP, Cavin1-meGFP was imaged using a conventional GFP filter cube (ET470/40, T495LPXR, ET525/50, Chroma). Using this filter cube does not allow spectral separation of the unconverted pool of mEos3.2 from the GFP fluorescent signal. For this reason, in the case of MEF Cavin1$^{-/-}$ cell line, we were able to detect caveolin1-based structures (scaffolds) with the unconverted pool of mEos3.2-caveolin1 (whose emission spectra is similar to the one of GFP).

Single molecule segmentation and tracking

A typical sptPALM experiment leads to a set of at least 4000 images per cell, analyzed to extract molecule localization and dynamics. Single molecule fluorescent spots were localized and tracked over time using a combination of wavelet segmentation and simulated annealing algorithms [130,131,132]. Under the experimental conditions described above, the resolution of the system was quantified to 59 nm (Full Width at Half Maximum, FWHM). This spatial resolution depends on the image signal to noise ratio and the segmentation algorithm [133] and was determined using fixed mEos3.2 samples. We analyzed 130 2D distributions of single molecule positions belonging to long trajectories (>50 frames) by bi-dimensional Gaussian fitting, the resolution being determined as 2.3 s_{xy}, where s_{xy} is the pointing accuracy.

For the trajectory analysis, cell contours were identified manually from Cav1-GFP or unconverted pool of mEos3.2-caveolin1 images. We analyzed trajectories lasting at least 260 ms (≥13 points) with a custom Matlab routine analyzing the mean squared

displacement (MSD), which describes the diffusion properties of a molecule, computed as (Eq. 1):

$$\mathrm{MSD}(t = n \cdot \Delta t) = \frac{\sum_{i=1}^{N-n} (x_{i+n} - x_i)^2 + (y_{i+n} - y_i)^2}{N - n} \quad \text{Eq.1}$$

where x_i and y_i are the coordinates of the label position at time $I \times \Delta t$. We defined the measured diffusion coefficient D as the slope of the affine regression line fitted to the n=1 to 4 values of the MSD ($n \times \Delta t$). The MSD was computed then fitted on a duration equal to 80% (minimum of 10 points, 200 ms) of the whole stretch by (Eq. 2):

$$\mathrm{MSD}(t) = \frac{4r_{\mathrm{conf}}^2}{3}(1 - \mathrm{e}^{-t/\tau}) \quad \text{Eq. 2}$$

where r_{conf} is the measured confinement radius and τ the time constant $\tau = (r_{conf}^2 / 3D_{conf})$. To reduce the inaccuracy of the MSD fit due to down sampling for larger time intervals, we used a weighted fit. Trajectories were sorted in 3 groups: immobile, confined and diffusive. Immobile trajectories were defined as trajectories with D<0.011 $\mu m^2.s^{-1}$, corresponding to molecules which explored an area inferior to the one defined by the image spatial resolution ~(0.05 µm)² during the time used to fit the initial slope of the MSD [69] (4 points, 80 ms): $D_{threshold}$=(0.059 µm)²/(4x4x0.02s)~0.011 $\mu m^2.s^{-1}$. To separate confined and diffusive trajectories, we used the time constant calculated τ for each trajectory. Confined and diffusive events were defined as trajectories with a time constant inferior and superior to half the time interval used to compute the MSD (100 ms) respectively.

Integrative modeling of Cav1/JAK1 complex

The three-dimensional (3D) structure of Cav1 was retrieved from the Protein Data Bank (PDB) using accession number 7SC0 [17]. A 3D model of JAK was constructed using the SWISS-MODEL platform (https://swissmodel.expasy.org/) based on the human sequence (UNIPROT P23458) and a structural template from PDBID 8EWY (JAK1-WT) [134,135]. The JAK1$\Delta^{1072\text{-}1154}$ variant was constructed by erasing all residues after position 1071. To elucidate the interaction between Cav1 and JAK1, we used HADDOCK version 2.4, adopting an "Information-Guided Docking" approach to model the complex for both Cav1-JAK1 WT and Cav1-JAK1$\Delta^{1072\text{-}1154}$ variant [136,137]. This method was designed to explore the potential binding modes between specific and functionally significant residues within each protein. T90-V94 of Cav1-CSD and F1057-H1072 of JAK1 were chosen for their roles in the signaling pathways investigated in this study. The docking protocol was executed in three distinct stages to enhance the fidelity of the model. The initial stage (it0) involved generating 1,000 preliminary docking decoys through rigid-body docking using distance constraints based on these key residues. Only decoys with the highest compatibility scores were advanced to the refinement phase (it1). During this stage, 200 models were selected for semiflexible refinement within the torsion angle space, incorporating a simulated annealing protocol that began with a high-temperature phase for global orientation optimization. This was followed by iterative adjustments of the side chains and backbone orientations at the interaction interface. The final adjustment phase (itw) deepened the refinement of these 200 models, focusing on the protein-protein interface through energy minimization techniques. This allowed for significant

conformational adjustments of both the side chains and backbone, enhancing the alignment of the model with potential real-world interactions.

After completing the docking simulations, we conducted a comprehensive analysis of 200 docking decoys generated during the itw' phase to gain insight into the binding modes, affinities, and potential interactions between Cav1 and JAK1. The evaluation metrics included docking scores, binding energy calculations, and BSA measurements. Models displaying lower binding energies were interpreted as indicative of more stable and favorable interactions. Increased BSA values suggest a more extensive interaction interface, correlating with stronger binding. Furthermore, we quantified the distances between potential pairwise contacts involving key residues T90-V94 in Cav1 and F1057-H1072 in JAK1. Residue-based statistics, including details such as the maximum, average, and minimum pairwise minimum distances, were collected to provide valuable insights into the spatial relationships between these critical residues. Models were assessed against criteria including a BSA threshold exceeding 1100 $Å^2$, a maximum pairwise distance of less than 40 Å, and a minimum distance of less than 14 Å. All models were required to demonstrate a negative binding energy and negative HADDOCK score to be considered viable. Models fulfilling these stringent conditions were further analyzed to ensure the robustness of our findings, with particular emphasis on the positioning of JAK-1 relative to the simulated membrane plane.

Statistics & Reproducibility

All analyses were performed using GraphPad Prism version 6.0 to 8.0, (GraphPad Software, La Jolla, CA, USA). Two- tailed (paired or unpaired) t-test and Kolmogorov-Smirnov-Tests were used when comparing only two conditions. For more than two conditions, Kruskal-Wallis test was used with Dunn′s multiple comparison test (when

comparing all conditions to the control condition). Significance of mean comparison is marked on the graphs by asterisks. Error bars denote SEM or SD. No statistical method was used to predetermine sample size. The experiments were not randomized and the Investigators were not blinded to allocation during experiments and outcome assessment.

Unless stated otherwise in figure legends, all representative results shown for immunolabelling and western blots, were performed at least three times independently with similar results.

Reporting summary

Further information on research design is available in the Nature Research Reporting Summary linked to this article.

Data availability

All data supporting the findings of this study are available from the corresponding authors on reasonable request.

Figure 1

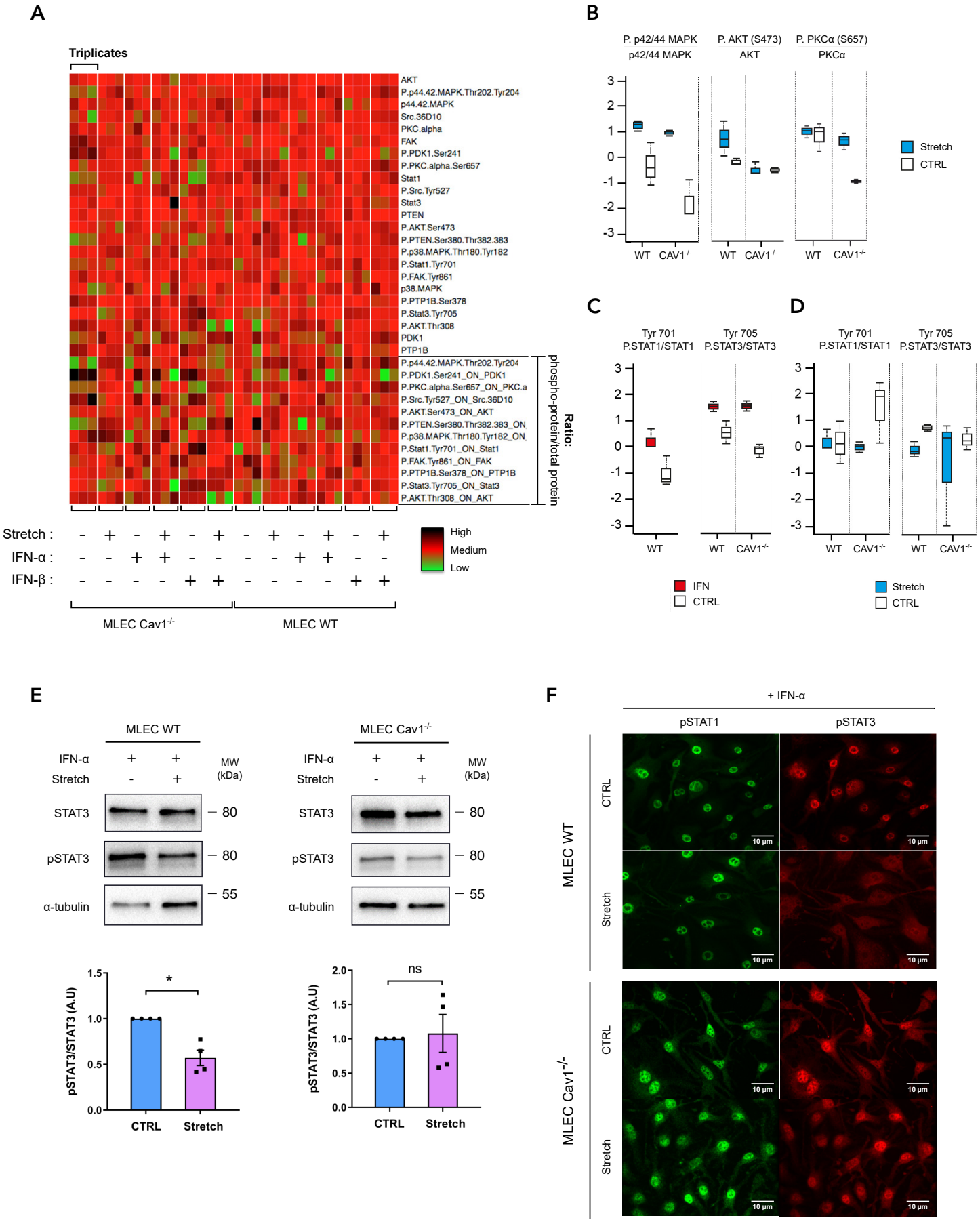

Figure 2

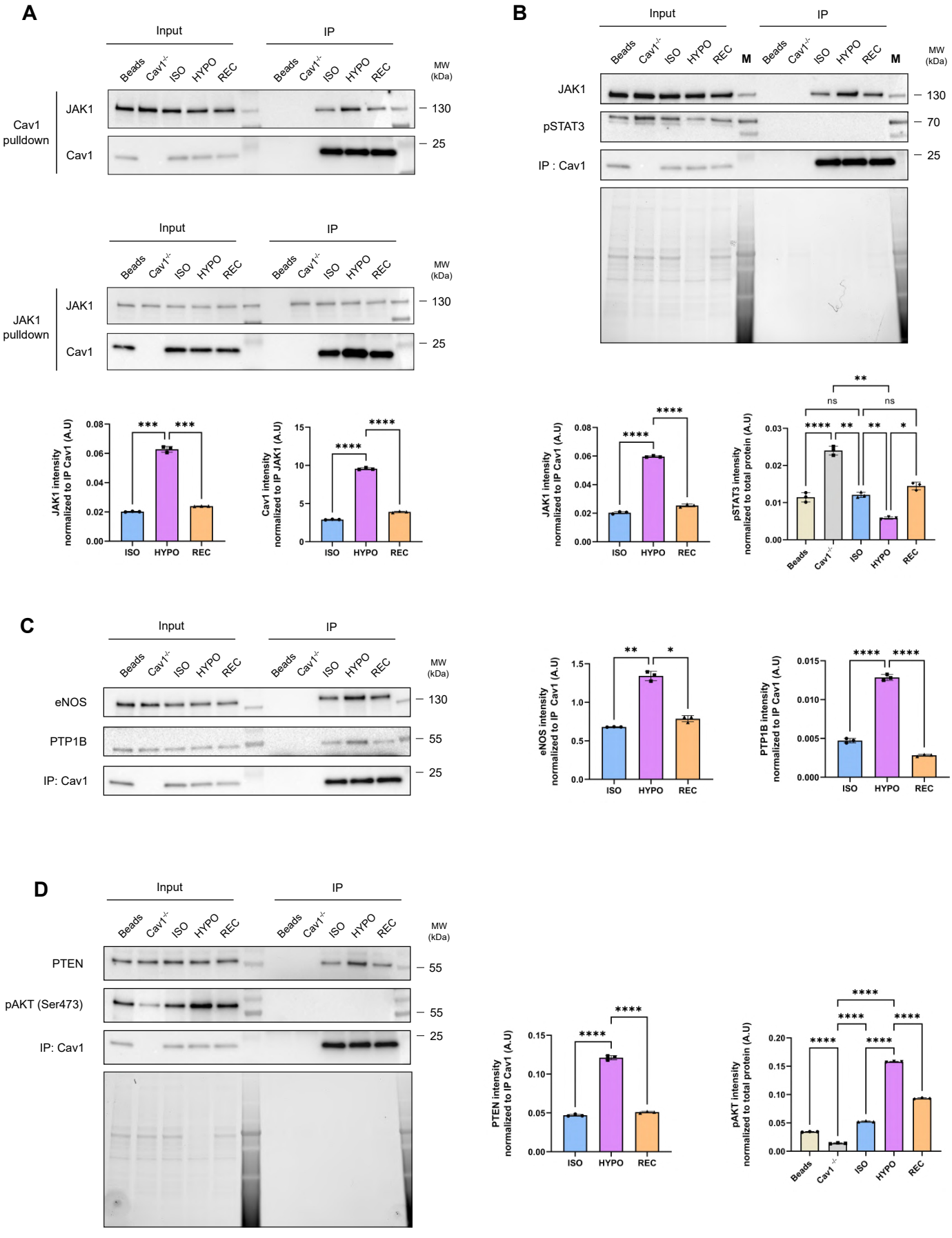

Figure 3

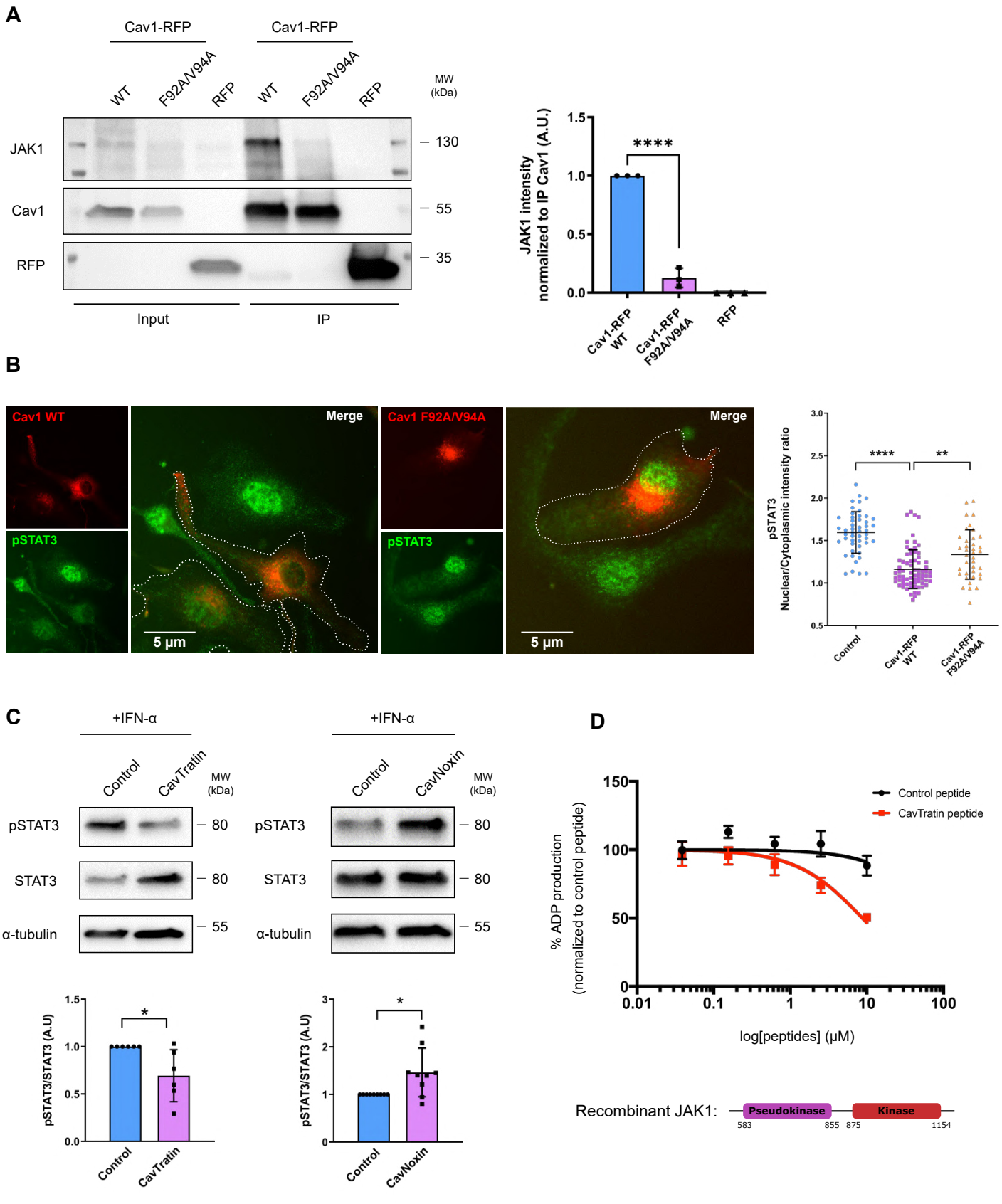

Figure 4

A

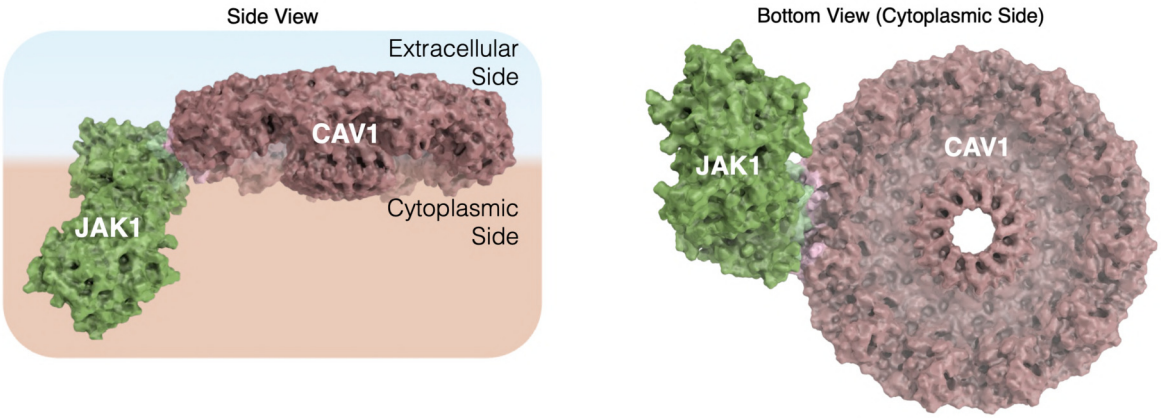

B

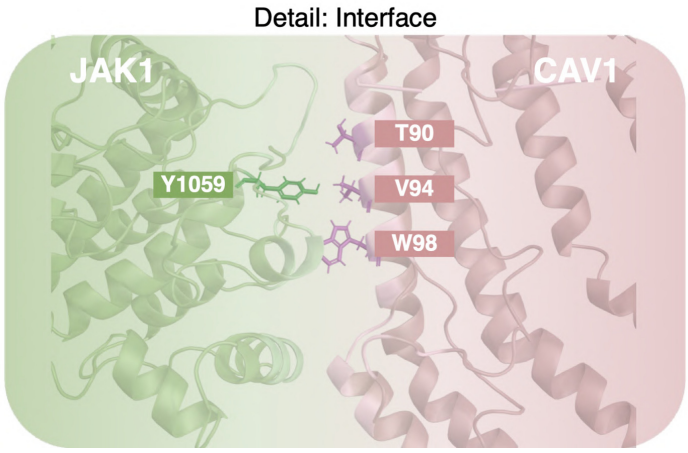

Figure 5

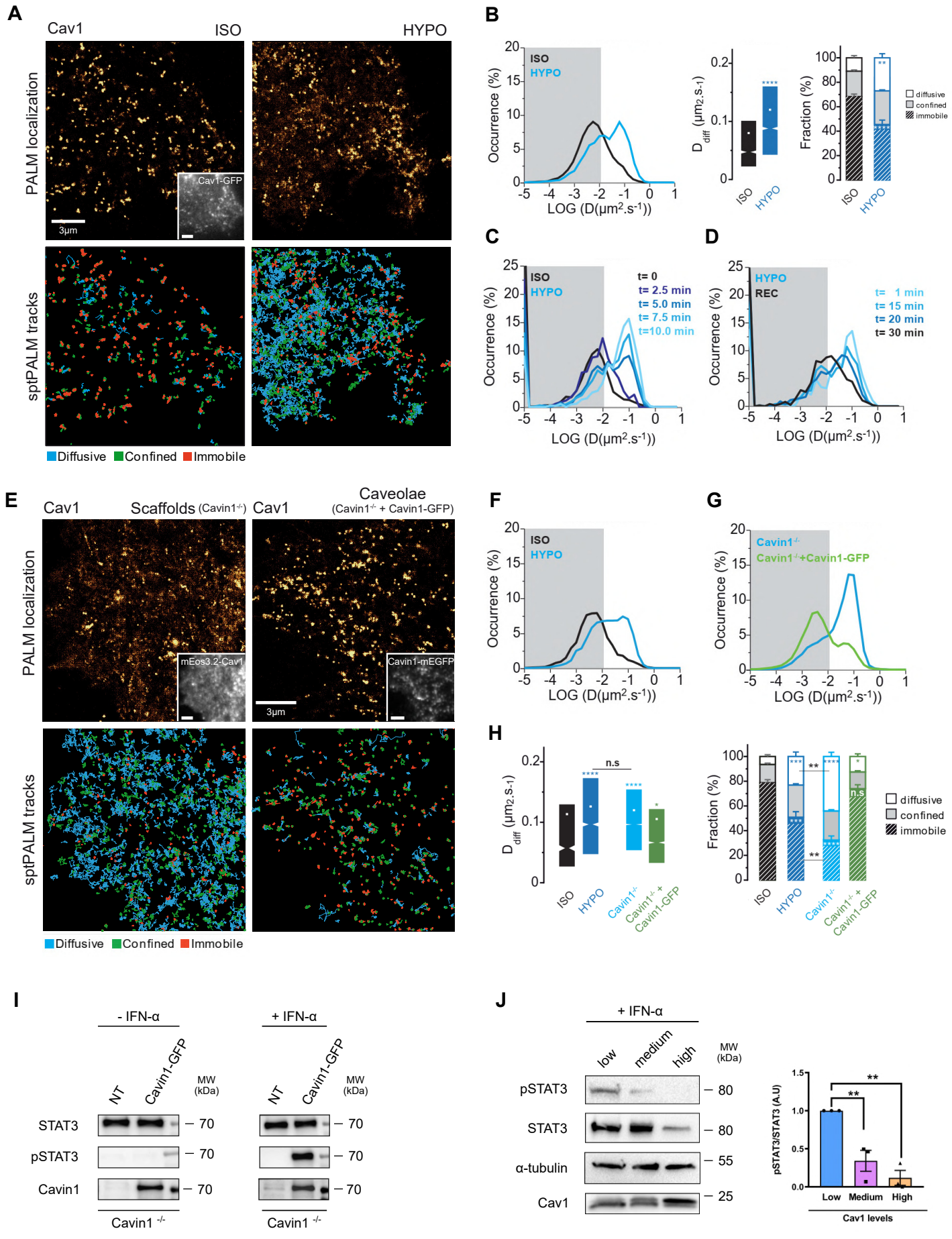

Figure 6

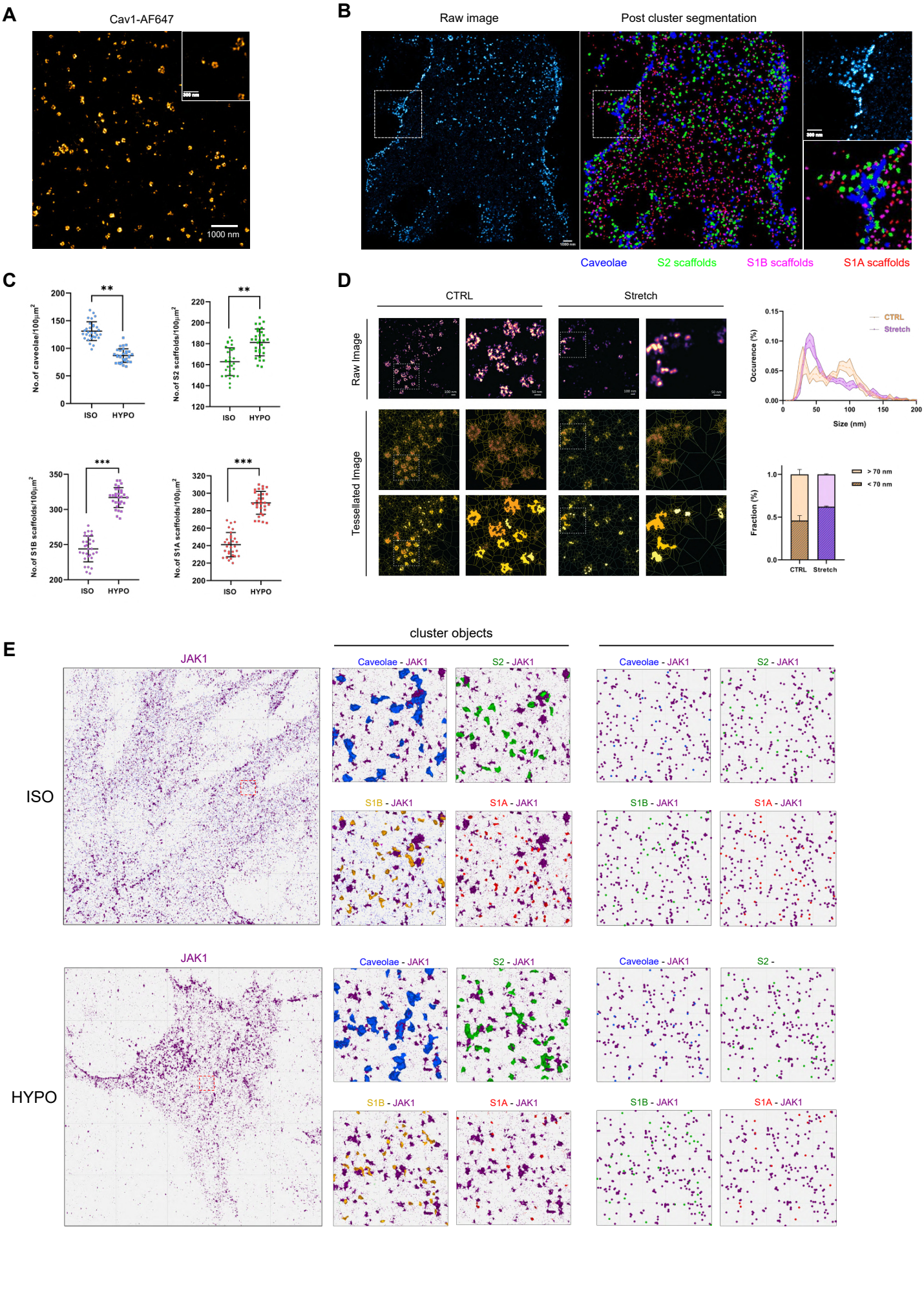

Figure 7

A

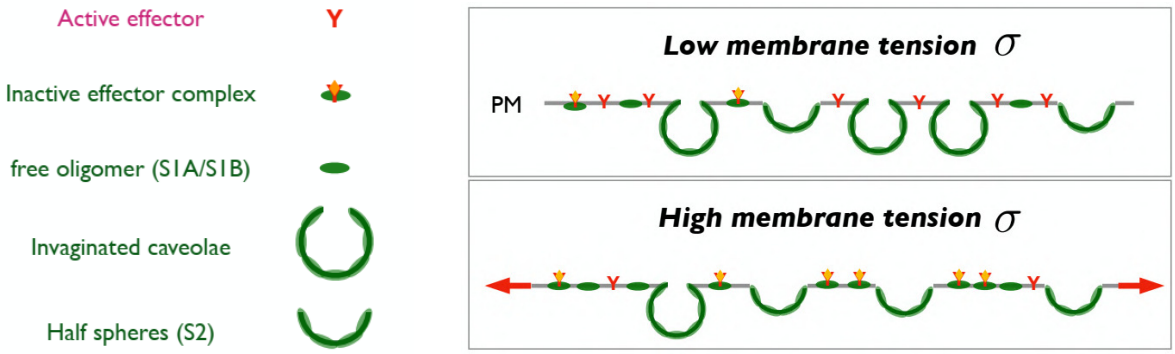

B

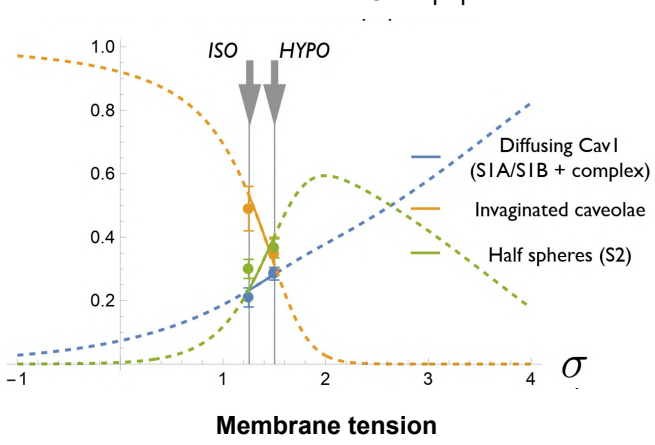

C